

Accreting SMBHs in the COSMOS field and the connection to their host galaxies

A. Bongiorno,^{1,2*} A. Merloni,¹ M. Brusa,¹ B. Magnelli,¹ M. Salvato¹ M. Mignoli,³ G. Zamorani,³ F. Fiore,² D. Rosario,¹ V. Mainieri,⁴ A. Comastri,³ C. Vignali,^{3,5} I. Balestra,¹ S. Bardelli,³ S. Berta,¹ F. Civano,⁶ P. Kampczyk,⁷ E. Le Floc’h,⁸ E. Lusso,⁹ D. Lutz,¹ L. Pozzetti,⁵ F. Pozzi,³ L. Riguccini,⁸ F. Shankar,¹⁰ and J. Silverman,¹¹

¹Max-Planck-Institut für extraterrestrische Physik (MPE), Giessenbachstrasse 1, D-85748, Garching bei München, Germany.

²INAF-Osservatorio Astronomico di Roma, Via di Frascati 33, 00040, Monteporzio Catone, Rome, Italy.

³INAF-Osservatorio Astronomico di Bologna, Via Ranzani 1, 40127, Bologna, Italy.

⁴ESO, Karl-Schwarzschild-Strasse 2, D85748 Garching bei München, Germany.

⁵Dipartimento di Astronomia, Università di Bologna, via Ranzani 1, I-40127 Bologna, Italy.

⁶Harvard Smithsonian Center for Astrophysics, 60 Garden Street, Cambridge, MA 02138, USA.

⁷Institute of Astronomy, ETH Zurich, CH-8093, Zurich, Switzerland.

⁸Laboratoire AIM, CEA/DSM-CNRS-Université Paris Diderot, IRFU/Service d’Astrophysique, Bât.709, CEA-Saclay, 91191 Gif-sur-Yvette Cedex, France.

⁹Max-Planck-Institut für Astronomie, Königstuhl 17, D-69117, Heidelberg, Germany.

¹⁰GEPI, Observatoire de Paris, CNRS, Univ. Paris Diderot, 5 Place Jules Janssen, F-92195 Meudon, France.

¹¹Institute for the Physics and Mathematics of the Universe (IPMU), University of Tokyo, Kashiwanoha 5-1-5, Kashiwa-shi, Chiba 277-8568, Japan.

Accepted Year Month Day. Received Year Month Day; in original form Year Month Day

ABSTRACT

Using the wide multi-band photometry available in the COSMOS field we explore the host galaxy properties of a large sample of Active Galactic Nuclei (AGN) (~ 1700 objects) with L_{bol} ranging from 10^{43} to 10^{47} erg s⁻¹ obtained by combining X-ray and optical spectroscopic selections. Based on a careful study of their Spectral Energy Distribution (SED), which has been parametrized using a 2-component (AGN+galaxy) model fit, we derived dust-corrected rest-frame magnitudes, colors and stellar masses of the obscured and unobscured AGN hosts up to high redshift ($z \lesssim 3$). Moreover, for the obscured AGN sample we also derived reliable star formation rates (SFRs). We find that AGN hosts span a large range of stellar masses and SFRs. No color-bimodality is seen at any redshift in the AGN hosts, which are found to be mainly massive, red galaxies. Once accounting for the color-mass degeneracy in well defined mass-matched samples, we find a residual (marginal) enhancement of AGN incidence in redder galaxies with lower specific star formation rates, and we argue that this result might emerge because of our ability to properly account for AGN light contamination and dust extinction, compared to surveys with a more limited multi-wavelength coverage. However, since these color shifts are relatively small, systematic effects could still be held responsible for some of the observed trend. Interestingly, we find that the probability for a galaxy to host a black hole growing at any given “specific accretion rate” (i.e. the ratio of X-ray luminosity to the host stellar mass) is almost *independent* of the host galaxy mass, while it decreases as a power-law with L_X/M_* . By analyzing the normalization of such probability distribution, we show how the incidence of AGN increases with redshift as rapidly as $(1+z)^4$, in close resemblance with the overall evolution of the specific star formation rate of the entire galaxy population. We do provide the analytic fitting formulae that describe the probability of a galaxy of any mass (above the completeness limit of the COSMOS survey) to host an AGN of any given specific accretion rate as a function of redshift. These can be useful tools for theoretical studies of the growing black holes population within galaxy evolution models. Although AGN activity and star formation in galaxies do appear to have a common triggering mechanism, at least in a statistical sense, within the COSMOS sample we do not find strong evidence of any ‘smoking gun’ signaling powerful AGN influence on the star-forming properties of their hosts galaxies.

Key words: Surveys, Catalogues, Galaxies:active, Galaxies: fundamental parameters, Galaxies: evolution

1 INTRODUCTION

Most of the times since their discovery, more than 40 years ago, Active Galactic Nuclei (AGN) powered by accretion onto Supermassive Black Holes (SMBH) have been considered rare and exotic objects with peculiar (and extreme) astrophysical properties. In the past decade, studies in the local Universe established the presence of supermassive Black Holes in the nuclei of virtually all galaxies with a bulge/spheroidal component (e.g. Kormendy & Richstone 1995; Kormendy & Bender 2011); changing dramatically the perception of this class of objects. Since cosmological SMBH growth is mostly due to accretion of matter during their active phases (Soltan 1982), we are led to conclude that most bulges went through a phase of strong nuclear activity (Marconi et al. 2004; Merloni & Heinz 2008; Shankar 2009). Moreover, as the energy released in the process of accretion on the SMBH can be higher than the total binding energy of a massive galaxy, AGN may represent a key ingredient of the formation and evolution of all galaxies. If, and how, the nuclear black holes influence their host galaxies, and vice-versa, became a major focus in studies of structure formation and evolution.

Indeed, many observational discoveries do support the notion of a close link between SMBH growth and the assembly of the host galaxy. The most crucial ones are the following: (i) The tight correlation between the central SMBH mass and various properties of their host galaxies i.e. luminosity: (Kormendy & Richstone 1995; McLure & Dunlop 2001; Marconi & Hunt 2003), stellar mass (Magorrian et al. 1998), and velocity dispersion (Ferrarese & Merritt 2000; Gebhardt et al. 2000; Tremaine et al. 2002; Kormendy & Bender 2011). (ii) As populations, SMBHs and galaxies seem to evolve with redshift in a similar way. In fact, the AGN evolution is luminosity-dependent with low-luminosity AGN reaching the peak in their space density later in the history of the Universe (i.e. at lower redshift) than higher luminosity AGN (Miyaji et al. 2000; La Franca et al. 2005; Ueda et al. 2003; Fiore et al. 2003; Cirasuolo et al. 2005; Hasinger et al. 2005; Bongiorno et al. 2007). This pattern is similar to the so-called “cosmic downsizing” of star forming galaxies (Cowie et al. 1996; Menci et al. 2008) seen also in the spheroidal galaxies (Cimatti et al. 2006; Thomas et al. 2010). (iii) The shape of the integrated AGN activity over cosmic time is similar to the one of the global star formation rate (SFR) with a peak at $z \sim 2$ and a rapid decline at both lower (e.g. Dickinson et al. 2003; Merloni 2004; Hopkins et al. 2007; Shankar et al. 2009) and higher (e.g. Franceschini et al. 1999; Wilkins et al. 2008; Brusa et al. 2009a) redshift. (iv) Finally, luminous AGN show a correlation between the AGN bolometric luminosity and the star formation (SF) of the host galaxy over more than five orders of magnitude in luminosity (Netzer 2009), albeit with a substantial scatter; possible deviation from such a behavior have however been reported for lower luminosity AGN (Shao et al. 2010; Mullaney et al. 2012; Santini et al. 2012).

While the evidences of a tight link between the formation of galaxies and the growth of the SMBHs at their centers are many and clear, the physical processes behind this interplay remain unclear. In particular, the fundamental question of whether AGN-driven feedback processes are ultimately responsible for determining global properties of the galaxy population (e.g. luminosity functions, color-magnitude distributions and the evolution thereof) or, on the contrary, they happen to be triggered and fueled as a by-product of star-formation activity and morphological evolution of their hosts still remains unanswered. This is of fundamental im-

portance for understanding both galaxy assembly and the accretion density of the Universe. The work we present here is indeed motivated by the desire to obtain robust, and statistically significant, constraints on the possible scenarios for the co-evolution of galaxies and AGN.

A slew of models (e.g. Somerville et al. 2001; Granato et al. 2004; Monaco & Fontanot 2005; Croton et al. 2006; Hopkins et al. 2006; Cen & Chisari 2011; Springel et al. 2005; Schawinski et al. 2006) have been developed in recent years to explain this co-evolution and to describe the main mechanism that fuel the central SMBH and build the galaxies’ bulge. Some of these semi-analytical models and hydrodynamical simulations (e.g. Springel et al. 2005; Hopkins et al. 2006; Menci et al. 2008) invoke major mergers of gas-rich galaxies as the main fueling mechanism. Alternative mechanisms have been discussed in the literature, including minor-mergers (e.g. Johansson et al. 2009), disk instabilities (e.g. Genzel et al. 2008), and recycled gas from dying stars (e.g. Ciotti et al. 2010). Different fueling mechanisms are usually associated to different luminosity ranges e.g. major mergers are invoked to trigger bright quasars (e.g. Hopkins et al. 2008), while the role of major mergers in triggering more typical ($\sim L_*$) AGN is called into question (see e.g. Cisternas et al. 2011; Schawinski et al. 2011; Kocevski et al. 2012). On the contrary, secular processes seem to be enough to fuel low luminosity AGN i.e. Seyfert-like objects (Hopkins et al. 2008; Allevato et al. 2011). Due to the large mismatch in physical scales between AGN and galaxies, all these models have to rely on specific assumptions regarding the mechanism responsible for the link between the nuclear activity, which releases most of its energy on the scale of few Schwarzschild radii R_S ($\sim 10^{-5}$ pc), and the stellar population on much larger scales (\sim a few kpc, some $\sim 10^8$ times R_S). This mechanism is in most cases an energetic feedback from the central engine that deposits the energy liberated by the accretion process within the host galaxy, or its dark matter halo (Silk & Rees 1998). The physical description of the feedback itself and its effect on the AGN host galaxy is, however, very different among different models.

In particular, due to the complex interplay between gas inflow, outflow and nuclear obscuration during active AGN phases, a correct and complete identification of unobscured, obscured, and highly obscured AGN at all redshifts (and especially in the $z = 1 - 3$ interval, where most of the feedback is expected to happen) is therefore crucial for a comprehensive understanding of the still little explored phase of the common growth of SMBHs and their host galaxies.

Generally speaking, two different approaches can be followed to test the predictions of different theoretical models of AGN feedback and to constrain the physical mechanisms at play: a detailed study of the physical properties of relatively small but well defined samples of selected sources or a statistical investigation of a large sample of AGN which includes different sub-classes. Within the COSMOS survey, the first approach has been followed in our previous papers (i.e. Merloni et al. 2010; Mainieri et al. 2011; Cisternas et al. 2011; Lusso et al. 2011), while the latter approach is adopted here.

To study growing SMBHs and their influence on the host galaxies over different periods of their cosmic evolution, one needs to compile a sample of AGN (both unobscured and obscured) as complete as possible, spanning a wide range in luminosity and redshift. X-ray surveys have been proved to be the most efficient way to compile nearly unbiased samples of Compton Thin AGN (Brandt & Hasinger 2005), but they may miss Compton thick AGN (e.g. Comastri & Brusa 2008; La Massa et al. 2009). On the other

hand, the optical spectroscopic selection, even though allowing a straightforward selection of unobscured AGN and being less biased against Compton Thick AGN, can fail to select those AGN for which the nuclear optical/IR light is diluted by their host galaxy. To overcome these limitations, we decided to consider and combine X-ray and optically selected AGN samples compiling a highly homogeneous and representative sample of obscured and unobscured AGN selected in the COSMOS field over a wide redshift baseline ($0 < z < 4$).

Other selections criteria (e.g. from IR color-color diagrams, Stern et al. 2005; Donley et al. 2012, or from radio surveys, e.g. Smolčić et al. 2008) may provide additional AGN and are needed in order to get a full picture on the AGN-galaxy co-evolution (e.g. Hickox et al. 2009). However, since X-ray and optical selections make up more than 50% of the full AGN population in COSMOS (Brusa et al. in prep) for the purpose of this paper we will focus on only these two methods quantifying, whenever relevant, the incompleteness due to the not inclusion of the other samples.

The major observational challenge in any comprehensive study of the AGN-galaxy co-evolution is the accurate separation of the AGN and galaxy emission components, at all optical-IR wavelengths. This is a crucial step for a number of reasons: depending on the intrinsic spectral energy distribution of the nuclear (AGN) and of the stellar light, and of their respective level of extinction, inaccurate de-blending might not only hamper any precise determination of the galaxies' physical properties, but also mask AGN signatures and bias our view of the SMBH growth.

To this end, we used a two-component Spectral Energy Distribution (SED) fitting procedure. The observed SED is fitted with a large grid of models based on a combination of the Richards et al. (2006) AGN template and several host-galaxy models (i.e. synthetic spectra created from the stellar population synthesis models of Bruzual & Charlot 2003). Given the wide multi-wavelength coverage available in the COSMOS field, this fitting technique allows to decompose, typically with a high level of confidence, the entire SED into nuclear AGN and host galaxy components and to derive robust measurements of the host galaxy physical properties, e.g. rest-frame colors, stellar mass, K-band luminosity and star formation rate. The strength of the SED fitting method is that, given sufficiently wide photometric coverage, it is applicable to all AGN, obscured and unobscured, independent of their luminosity. In particular, once a comprehensive set of templates for the SED components is chosen, the method can be applied (almost) blindly to any detected object in a multi-wavelength survey, irrespective of the specific selection criteria, reaching an accuracy that depends crucially on the number of bands and depth of the available photometric catalogs. In this respect, COSMOS is a uniquely suited field for our investigation.

The structure of the paper is as follows: In Section 2 we will introduce our sample, before proceeding to a discussion of the 2-component SED fitting method in Section 3. In Section 4 we will discuss the physical properties of the AGN host galaxies (i.e. colors, masses and SFRs) compared to normal galaxies focusing in Section 4.3 and 4.4 on the incidence of the AGN as a function of their host properties i.e. mass and star-formation rate, respectively. A final discussion and a summary of our main results are presented in Section 5 and 6. Additionally, in Appendix A we discuss the effect on the derived host galaxy properties if the AGN component is not properly subtracted, while Appendix B shows a detailed comparison between two SFR indicators i.e. UV-optical SED fitting and the FIR bands based method. In Appendix C two tables with the AGN catalog and the parameters derived from the SED fitting (e.g.

rest-frame magnitudes, masses and SFRs) can be found together with a short explanation of the columns. These tables show only 16 lines as an example of the ones published online. Throughout this paper, we use the standard cosmology ($\Omega_m=0.3$, $\Omega_\Lambda=0.7$, with $H_0=70 \text{ km s}^{-1} \text{ Mpc}^{-1}$). Magnitudes, if not differently specified, are AB magnitudes.

2 AGN SAMPLES FROM THE COSMOS SURVEY

In order to construct a sample of AGN as complete as possible, including both obscured and unobscured objects, we first selected XMM-COSMOS point-like sources (Hasinger et al. 2007; Cappelluti et al. 2009), to which we added a smaller sample of purely optically selected AGN from the zCOSMOS bright spectroscopic survey (Lilly et al. 2009), spanning a lower AGN luminosity range (Bongiorno et al. 2010, Mignoli et al. in prep). In this section, we give the details of our sample selection.

2.1 The X-ray selected sample

The XMM-COSMOS catalog includes ~ 1800 point-like X-ray sources. The X-ray catalog has been presented in Cappelluti et al. (2009), while the optical identifications and multi-wavelength properties have been discussed in Brusa et al. (2010)¹. The sources of the XMM-COSMOS catalog of Brusa et al. (2010) have been classified as normal galaxies, obscured and unobscured AGN according to their properties, i.e. X-ray luminosities, spectra and multi-wavelength SEDs (Salvato et al. 2011); here we consider only those sources classified as AGN, both unobscured and obscured, as we describe below.

Optical spectra are available for more than half of the sample from different instruments: VIMOS/VLT (zCOSMOS project, Lilly et al. 2007, 2009), IMACS/Magellan (Trump et al. 2007, 2009), MMT (Prescott et al. 2006), and DEIMOS/KeckII (P.I. Scoville, Capak, Salvato, Kartaltepe, Mobasher).

From the XMM-COSMOS subsample for which spectra are available, we identified 430 sources which show broad ($\text{FWHM} > 2000 \text{ km s}^{-1}$) emission lines in their optical spectra, which we classify as type-1 (unobscured). Further 402 spectroscopically confirmed AGN were instead classified as type-2 (obscured), by making use of both their spectral properties and X-ray luminosities. In particular, the type-2 AGN class includes: (a) all the sources that do not show broad emission lines and for which the ratio between their high-ionization narrow lines indicates AGN activity (Baldwin et al. 1981) and (b) in case the high ionization lines are not detected in the observed wavelength range, all the objects without broad lines and with rest-frame (2-10 keV) X-ray luminosity greater than $2 \times 10^{42} \text{ erg s}^{-1}$.

For about half of the XMM-COSMOS sources (723 objects), only photometric redshifts are available (the “photo-z” AGN sample), which are however very accurate with $\sigma_{\Delta z/(1+z)} \sim 0.015$ and a fraction of outliers of just 5.8% (Salvato et al. 2009, 2011). Thus, the XMM-COSMOS sources for which no spectra are available

¹ In this paper we use an improved version of the XMM-COSMOS identifications catalog with respect to the one published in Brusa et al. (2010), the main difference being the availability of new photometric redshifts from Salvato et al. (2011). The updated version of the XMM-COSMOS identification catalog can be downloaded here: http://www.mpe.mpg.de/XMMCosmos/xmm53_release/

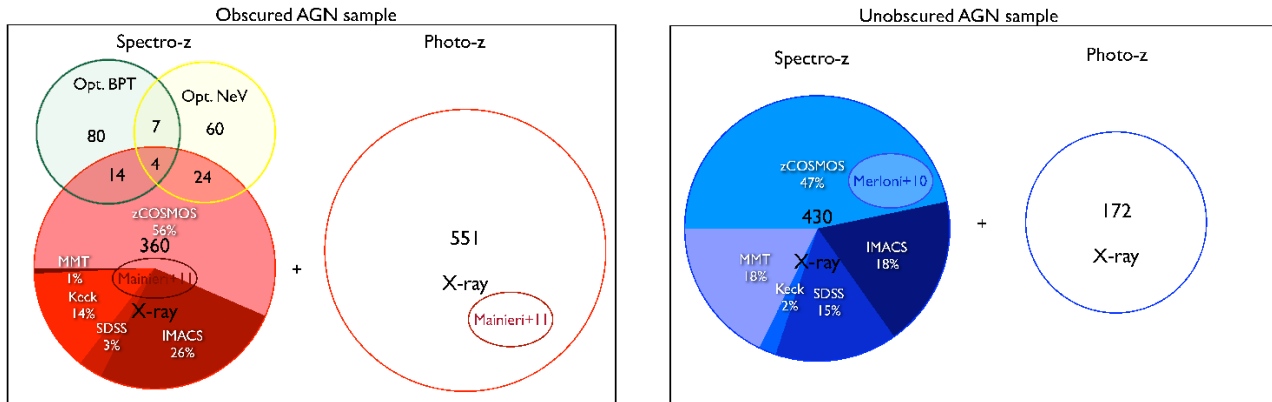


Figure 1. Schematic view of the analyzed sub-samples for obscured (left) and unobscured (right) AGN. Different circles represent the different methods used to select them. Blue and red circles correspond to X-ray unobscured and obscured AGN, green and yellow to optically selected AGN using the diagnostic diagrams and the [Ne v] line. Open and filled symbols are for photometric and spectroscopic redshift whose origin is highlighted with the slices of different color gradations. The combined analyzed sample consists of 1702 AGN: 602 type-1 AGN (of which 430 with spectra) and 1100 type-2 AGN (of which 549 with spectra).

Obscured AGN sample				
	Spec-z		Phot-z	
	X-ray	OptBPT	OptNeV	Xray
X-ray	360	18	28	551
OptBPT	18	105	11	
OptNeV	28	11	95	

Unobscured AGN sample		
	Spec-z	Phot-z
X-ray	430	172

Table 1. Analyzed sub-samples of obscured and unobscured AGN. Bold numbers indicate the total number of sources while the rest highlight the sources in common between two or more classification methods. The combined analyzed sample consists of 1702 AGN: 602 unobscured AGN (of which 430 with spectra) and 1100 obscured AGN (of which 549 with spectra).

have been classified as unobscured type-1 in 172 cases, and as obscured type-2 in 551 cases. In practice, the source classification for “photo-z” AGN was performed as in Salvato et al. (2011) on the basis of the template² that best describes their SED, and applying the same threshold in X-ray luminosity ($L_{[2-10]keV} > 2 \times 10^{42}$ erg s⁻¹).

Summarizing, the XMM-COSMOS sample analyzed in this work comprises 602 unobscured type-1 AGN (430 with spectroscopic redshift and broad emission lines; 172 with photometric redshift) and 953 obscured type-2 AGN (402 with spectroscopic redshift and 551 with photometric redshift), for a total of 1555 X-ray selected AGN.

² chosen from a library of hybrid template obtained combining the observed galaxy templates from Polletta et al. (2007) with different levels of AGN contamination (Salvato et al. 2011)

2.2 Optically selected Seyfert-2 galaxies: diagnostic diagrams

For type-1 AGN the X-ray and optical selection match very well, i.e. in addition to the 430 spectroscopic broad line AGN with XMM detection, there are only 25 (~6%) objects purely optically selected from the zCOSMOS bright survey which are not detected in the X-ray band by XMM (the number goes down to just 14, ~3%, if we consider also Chandra detections). This is not the case for obscured type-2 AGN, for which a more substantial fraction (>25%) can be selected from optical surveys showing no X-ray counterparts. Moreover, while the redshift and luminosity distribution of X-ray and optically selected type-1 AGN is very similar, for type-2 objects this is not the case and different bands can allow us to retrieve different sub-classes of sources. For this reasons, we include in this study also obscured type-2 AGN selected purely on optical properties. Since optically selected AGN (Seyfert-2 galaxies) tend to have much lower luminosities (Fig. 10) this allows us to enlarge the analyzed luminosity range.

The sample of optical type-2 AGN was selected in the following way: from the final 20 000 VIMOS/VLT zCOSMOS bright, and in analogy with the procedure adopted in Bongiorno et al. (2010) for the first 10 000 spectra (10k, Lilly et al. 2009), we have selected 392 sources using the standard diagnostic diagrams ([O III]/H β versus [N II]/H α and [O III]/H β versus [S II]/H α , Baldwin et al. 1981, BPT diagram) to isolate AGN in the redshift range $0.15 < z < 0.45$ and the diagnostic diagram [O III]/H β versus [O II]/H β (Rola et al. 1997; Lamareille et al. 2004, “blue” diagram) to extend the selection to higher redshift ($0.5 < z < 0.92$). These diagnostic diagrams allow the classification of emission line objects as Seyfert-2 galaxies, candidate Seyfert-2 galaxies, and LINERs. Here we include only the 105 objects classified as secure Seyfert-2 galaxies (the LINER sample is studied separately in Tommasin et al. 2012). Of these 105 AGN, 18 have X-ray counterparts and therefore are already included in the X-ray selected sample described above. Hence, from the optical selection based on the spectral diagnostic diagrams, we isolated 87 pure optically selected Seyfert-2 which do not show any X-ray emission at the depth of our XMM observations.

2.3 Optically selected obscured AGN: the [Ne v] emission line sample

A relatively new method to select obscured AGN in the optical surveys uses the detection of [Ne v] line whose presence is a distinctive feature of AGN activity (see e.g. Gilli et al. 2010). Using this criterion on the same 20 000 zCOSMOS bright spectra, Mignoli et al. (in prep) identified 95 obscured type-2 AGN, 11 of which were already identified through the emission line diagnostic diagrams. Of the remaining 84 sources, 24 have X-ray counterparts and are hence already included in the X-ray selected sample described above. From the [Ne v]-based optical selection, we thus isolated additional 60 pure optically selected Seyfert-2 which do not show any X-ray detection.

In total, the optically selected obscured AGN amount to 189 sources, of which 147 are purely optically selected with no XMM detection³. Since both these two criteria are based on spectral features, the number of spectra available for obscured AGN is artificially higher than for the unobscured ones.

2.4 The total AGN sample and the parent galaxy sample

The final combined sample analyzed in this paper consists of 1702 AGN: 602 type-1 AGN (of which 430 with optical spectra) and 1100 type-2 AGN (of which 549 have spectra). A graphical representation of the sample and its basic substructure, highlighting classification, the method used, and overlaps among the various sub-samples, is shown in Figure 1 and in table 1. The color code adopted in Fig. 1 will be used throughout the entire paper: blue and red colors will denote X-ray unobscured and obscured AGN, respectively; green those Seyfert-2 galaxies selected optically using the diagnostic diagrams, and yellow the obscured AGN selected via [Ne v] line emission. Open and filled symbols are used instead for photometric and spectroscopic redshifts, respectively. The full sample can be found in the online material. An example of the published table is given in Table C1.

Since the aim of this work is to study the AGN host galaxy properties and compare them to normal galaxies, throughout this paper we will use the IRAC selected galaxy sample in the COSMOS area as comparison “parent” galaxy sample. For the whole galaxy sample photometric redshifts, masses and star-formation rates are available (Ilbert et al. 2010). Moreover, in order to disentangle multiple dependencies and thus isolate the real differences in the properties of galaxies hosting an AGN from those that do not, we have also created two *matched* parent samples: a “mass-matched parent sample” and an “i-band-apparent-magnitude-matched parent sample”. In both cases we matched each AGN with 3 non-AGN chosen from the whole IRAC sample. For the mass-matched sample we considered the (z, M) plane and for each AGN with a given redshift and host galaxy stellar mass (see section 3.5.1 below) we extracted the 3 non-AGN objects from the parent sample which lie closest in the (z, M) plane to the AGN allowing as maximum difference a factor of 10 in Mass. The same procedure was followed to build the I-band matched sample, this time working on the (z, i) plane, allowing as maximum difference a factor of 4 in luminosity.

³ We note here that 7 of the 147 purely optically selected AGN are actually detected in the deeper Chandra observation covering the central part of the COSMOS field (Elvis et al. 2009, Civano et al. in prep). In order to keep selection effects under control and exploit the full 2 deg² area of COSMOS, in this paper we limit the X-ray analysis to the XMM-COSMOS sample.

2.5 Multi-wavelength observations

The Cosmic Evolution Survey (COSMOS) is a multi-wavelength observational project over 1.4×1.4 deg² of equatorial field centered at $(RA, DEC)_{J2000} = (150.1083, 2.210)$ (Scoville et al. 2007). The COSMOS field is characterized by an unprecedented deep multi-wavelength coverage, and in order to compile the SED for the AGN sample described above, we exploited such a large number of multi-wavelength data available in the field. For most of the sources we have constrained the SED using 14 different bands that encompass optical to MIR wavelengths. More specifically, for all our sources we used 6 SUBARU bands (B, V, g, r, i, z; from Taniguchi et al. 2007), and the CFHT/ U-, J- and K-bands (Capak et al. 2007; McCracken et al. 2010). All but a few (~97%) of our sources are detected in all 4 Spitzer/IRAC bands (3.6 μ m, 4.5 μ m, 5.8 μ m and 8.0 μ m; Sanders et al. 2007; Ilbert et al. 2010) and ~80% of them are also detected in the 24 μ m Spitzer/MIPS band (Le Floch et al. 2009). For most of the sources we can thus constrain the SED in a very large wavelength interval, ranging from ~3800 Å(U_{CFHT}) to 24 μ m (Spitzer/MIPS). Moreover, for a few percent of the sample we can also rely on longer wavelength detections. In particular, for the X-ray selected sample, 109 sources have detection at 70 μ m (Spitzer/MIPS, Sanders et al. 2007), 216 are visible at 100 μ m and 201 at 160 μ m (77 of them are detected in both wavelengths) by the *Herschel* Space Observatory as part of the PACS Evolutionary Probe (PEP⁴; Lutz et al. 2011) guaranteed time key program.

3 SPECTRAL ENERGY DISTRIBUTIONS OF COSMOS AGN

In this section, we describe the main tool in our analysis, namely the study of the overall Spectral Energy Distribution of the entire AGN sample. The approach we follow is to consider, with as little *a priori* assumptions as possible, each and every observed SED in the sample as the result of the superposition of the nuclear AGN emission and of the galactic stellar light entering the fixed apertures of 3” diameter used to derive all optical/IR photometry (Salvato et al. 2009).

The typical SED of a pure QSO, shown in the right panel of Fig. 2, is characterized by two bumps in the UV and IR regimes (Sanders et al. 1989; Elvis et al. 1994; Richards et al. 2006) which create a dip at around 1 μ m. The UV bump is interpreted as thermal emission from the accretion disk (Czerny & Elvis 1987), while the IR bump is thought to be due to absorption of intrinsic AGN UV, X-ray and optical radiation by dusty clouds in the AGN ‘torus’ on ~pc-scales, which subsequently re-radiate this energy at IR frequencies (Barvainis 1987). Despite the apparent large scatter in the observed SED of large QSO/AGN samples (Richards et al. 2006), there appear to be little evidence for substantial systematic changes in the *shape* of such intrinsic SED (apart from those introduced by dust extinction) across wide luminosity ranges, as recently demonstrated by the analysis of broad H α line selected local AGN from the SDSS (DR7) survey (Stern & Laor 2012).

On the other hand, the optical SED of a galaxy (see e.g. left panel of Fig. 2) is usually modeled as due to the integrated light of the stellar populations of the galaxy which are generated by different star-formation histories. Galaxy SEDs peak typically at around 1 μ m for a very wide range of SFR histories.

In most AGN (with the exception of the most luminous ones)

⁴ <http://www.mpe.mpg.de/ir/Research/PEP>

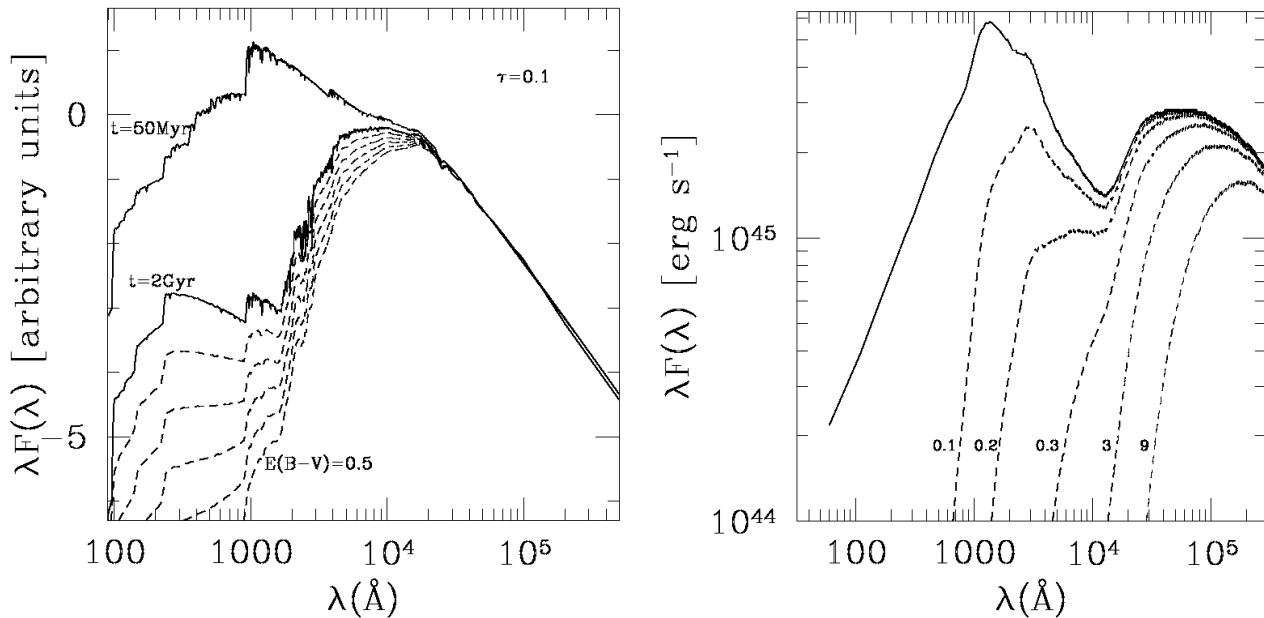


Figure 2. *Left:* Examples of galaxy templates derived from Bruzual & Charlot (2003) models. The two solid curves correspond to a model with $\tau=0.1$ and with ages of 50 Myr and 2 Gyr, respectively. The dashed curves correspond to the latter SED dust-reddened using Equation 3 with $E_g(B-V)=[0.1, 0.2, 0.3, 0.4, 0.5]$. *Right:* AGN template by Richards et al. (2006) (solid line). The dashed curves correspond to the same SED dust-reddened using Equation 4 with different $E_g(B-V)$ values [0.1, 0.2, 0.3, 3, 9].

both components significantly contribute and the global SED is the result of the combination of the central QSO’s and the host galaxy’s SED (Hao et al. 2009; Merloni et al. 2010; Lusso et al. 2011). How much these two components contribute to the global SED in detail depends on a number of factors, the most important ones being their relative luminosity and the level of obscuration affecting each of them.

3.1 Modeling the AGN and host galaxy emission components with SED fitting

Fixing the redshift of the source to the spectroscopic or photometric redshift, we fit the observed fluxes f_{OBS} with a two-component model using a combination of AGN and host-galaxy templates (see e.g. similar approaches Pozzi et al. 2010; Lusso et al. 2011) (but see Appendix A for a comparison with the standard SED fitting method without the AGN component). This fitting technique, initially presented in Bongiorno et al. (2007), has been already successfully used in the analysis of smaller AGN sub-samples in the COSMOS field (i.e. Merloni et al. 2010; Mainieri et al. 2011). More complex analysis, including multiple dust emission components, have been carried out by Lusso et al. (2012). As we mentioned before, the AGN and galaxy SEDs are shaped in a way that allows a relatively easy decoupling with the galaxy’s emission peak falling in the wavelength range of the AGN dip at $\sim 1\mu\text{m}$ (rest frame). To be specific, we assume that:

$$f_{\text{obs}} = c_1 f_{\text{AGN}} + c_2 f_{\text{GAL}} \quad (1)$$

Using a library of galaxy and AGN templates we find the best normalization parameters c_1 and c_2 that reproduce the observed flux of each object, by minimizing the χ^2 . In type-1 unobscured AGN, we expect the AGN component to dominate in the optical and IR

bands with some degree of contribution from the host galaxy, while the optical continuum of type-2 obscured AGN is dominated by the host galaxy emission with the AGN component rising mainly at IR wavelength. Notice that we are not implying that both components are always detectable. Solutions in which the SED is a pure QSO (in case of type-1 AGN) or a galaxy with a negligible contribution from the central AGN (in case of type-2 AGN) are both possible.

3.2 Library templates

The data are fitted with a large grid of AGN and galaxy templates. For the AGN component we adopt the Richards et al. (2006) mean QSO SED as derived from the study of 259 IR selected quasars with both Sloan Digital Sky Survey and Spitzer photometry (see right panel of Fig. 2). The Richards SED is an extension and is consistent with the original Elvis et al. (1994) QSO SED. For the galaxy component we generated a library of synthetic spectra using the models of stellar population synthesis of Bruzual & Charlot (2003). We assumed a universal initial mass function (IMF) from Chabrier (2003) and we built 10 exponentially declining star formation histories (SFH) $SFR \propto e^{-t_{\text{age}}/\tau}$ with e-folding times, τ , ranging from 0.1 to 30 Gyr and a model with constant star formation. For each of the SFHs, the SED was generated for a grid of 13 ages ranging from 50 Myr to 9 Gyr, subject only to the constraint that the age should be smaller than the age of the Universe at the redshift of the source. Some examples of the used galaxy templates are given in the left panel of Fig. 2.

3.2.1 Extinction

Both the AGN and the galaxy templates can be affected by dust extinction. The observed flux can be written as

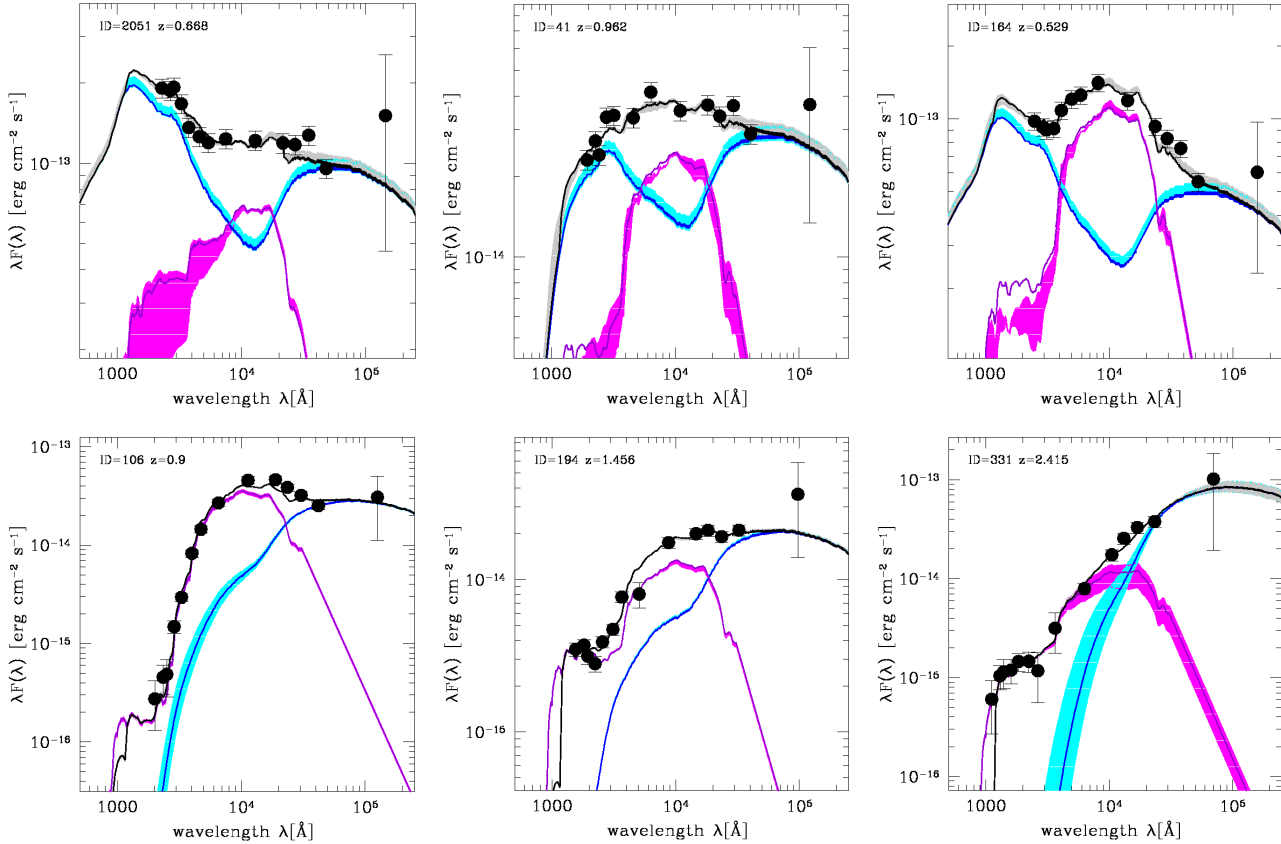


Figure 3. Examples of SED decompositions for unobscured AGN (upper panels) and obscured ones (bottom panels). Black circles are rest-frame fluxes corresponding to the observed bands used to constrain the SED. Purple and blue lines correspond to the galaxy and the AGN template found as best-fit solution through the χ^2 minimization, while the black line shows their sum. Pink and cyan shaded areas show the range of the SED template library within 1σ of the best-fit template, and light gray their sum.

$$f_{\text{obs}}(\lambda) = f_{\text{int}}(\lambda) \times 10^{-0.4A_\lambda}, \quad (2)$$

where f_{obs} and f_{int} are the observed and the intrinsic fluxes, respectively, and A_λ is the extinction at a given wavelength λ described by $A_\lambda = k(\lambda)E(B - V)$, with the color excess $E(B - V)$ and the reddening curve $k(\lambda)$.

Galaxies:

Recent studies on high redshift galaxies and star formation obscured by dust have shown the importance of the reddening in the high- z universe. Therefore, dust extinction, produced inside the galaxies themselves, is an important effect to be taken into account.

We chose as reddening curve for our galaxy templates the Calzetti's law (Calzetti et al. 2000), which is the most used attenuation curve in high-redshift studies. The Calzetti's law is an empirical relation derived using a small sample of low-redshift starburst galaxies (SB) and has the following form:

$$k_g(\lambda) = \begin{cases} 2.659 \left(-2.156 + \frac{1.509}{\lambda} - \frac{0.198}{\lambda^2} + \frac{0.011}{\lambda^3} \right) + R_V \\ 2.659 \left(-1.857 + \frac{1.040}{\lambda} \right) + R_V \end{cases} \quad (3)$$

with $R_V = 4.05$. The two equations are valid for $0.12 \mu\text{m} \leq \lambda \leq 0.63 \mu\text{m}$ and $0.63 \mu\text{m} \leq \lambda \leq 2.20 \mu\text{m}$, respectively. Below and

above the valid wavelength range, the slope is computed extrapolating to lower and higher wavelengths the value of $k_g(\lambda)$ obtained by interpolating between $0.11 - 0.12 \mu\text{m}$ and $2.19 - 2.20 \mu\text{m}$, respectively.

In the fitting procedure we considered for the galaxy component only $E_g(B - V)$ values in the range $0 \leq E_g(B - V) \leq 0.5$. Following Fontana et al. (2006) and Pozzetti et al. (2007), we impose the prior $E_g(B - V) < 0.15$ if $t_{\text{age}}/\tau > 4$ (i.e. we excluded the models implying large dust extinctions in the absence of a significant star formation rate, $t_{\text{age}}/\tau > 4$).

In the left panel of Fig. 2 we show two examples of galaxy templates with $\tau=0.1$ and $t_{\text{age}}=50\text{Myr}$, 2Gyr (solid lines). For the latter template we also show the corresponding dust-reddened templates obtained by applying the above equations with different $E_g(B - V)$ values (dashed lines).

AGN:

The extinction of the nuclear AGN light has been modeled with an SMC-like dust-reddening law from Prevot et al. (1984) for which:

$$k_a(\lambda) = 1.39 \lambda_{\mu\text{m}}^{-1.2} \quad (4)$$

We considered $E_a(B - V)$ values in the range $0 \leq E_a(B - V) \leq 1$ for unobscured type-1 AGN and $0.3 \leq E_a(B - V) \leq 9$ for the obscured ones, in steps of $\Delta E_a(B - V) = 0.1$. In the right panel of Fig.

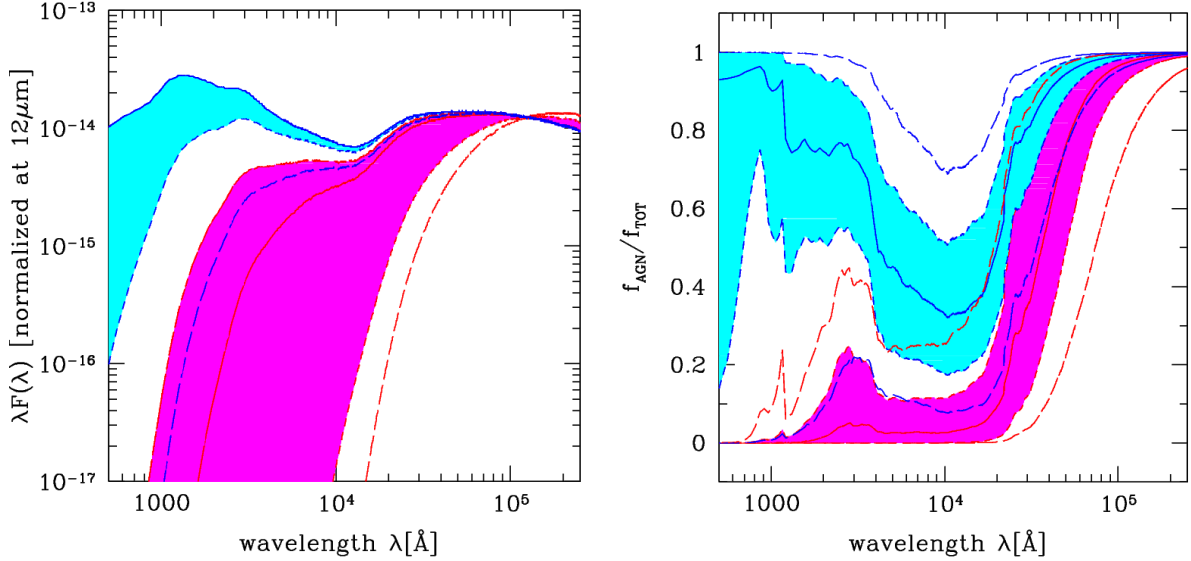


Figure 4. *Left Panel:* Median AGN SED chosen as best fit for our sample of unobscured (blue continuum line) and obscured (red continuum line) AGN, all normalized at rest-frame $12\mu\text{m}$. Shaded areas correspond to the range within 25th and 75th percentiles, while long dashed lines that within the 10th and 90th percentiles. *Right:* Median AGN contribution to the total SED at different wavelengths for unobscured (blue continuum line) and obscured (red continuum line) AGN. Shaded areas correspond to the range within the 25th and 75th percentiles, while long dashed lines that within the 10th and 90th percentiles.

2 we show the AGN template (solid line) and the corresponding dust-reddened templates obtained for different $E_a(B-V)$ values. As visible in this figure, the upper limit of $E_a(B-V) = 9$ corresponds to a very extinct AGN SED, and an even higher upper limit would not change by much the SED shape.

Taking into account the described extinction laws, we can rewrite Eq. 1 as

$$f_{\text{obs}} = c_1 f_{\text{AGN}}^{\text{int}}(\lambda) \times 10^{-0.556 \lambda_{\mu\text{m}}^{-1.2} E_a(B-V)} + c_2 f_{\text{GAL}}^{\text{int}}(\lambda) \times 10^{-0.4k_g(\lambda) E_g(B-V)} \quad (5)$$

with $k_g(\lambda)$ described by Eq. 3

3.3 Results of the SED fitting

Given the wide multi-wavelength coverage, the fitting technique described above allows to decompose the entire spectral energy distribution into a nuclear AGN and a host galaxy component and to derive robust measurements of both the AGN and the host galaxy properties, for almost all (98.6%) of the objects in the original sample⁵. Some examples of the SED fitting for unobscured (upper panels) and obscured AGN (bottom panels) are shown in Figure 3, while the left panel of figure 4 shows the median SED chosen as best fit in the sed fitting for unobscured (blue) and obscured (red) AGN together with the 10th, 25th, 75th and 90th percentiles of the samples. Finally, the right panel of the same figure highlights the median AGN contribution to the global SED at different wavelengths for unobscured (blue continuum line) and obscured (red

continuum line) AGN. Again the shaded areas and the long dashed lines mark the 10th, 25th, 75th and 90th percentiles of the samples, respectively. From this figure, we see that, for obscured AGN, three quarters of the objects have AGN contribution in the optical bands smaller than 20%. Thus, any residual AGN contamination (or AGN over-subtraction), should not affect the determination of the rest-frame optical colors of the host by more than about 0.1 magnitude. On the other hand, at rest-frame wavelengths of about $1\mu\text{m}$, three quarters of type-1 AGN have AGN fractions smaller than about 50%, implying that, even for unobscured objects, our method allow a robust determination of the host total stellar masses (see also Merloni et al. 2010).

Based on the best fit solution we derived the AGN luminosity and the galaxies' rest-frame magnitudes, colors, stellar mass content and star formation rate. One sigma errors on the best fit parameters are computed considering the range of values corresponding to the solutions for which $\Delta\chi^2 = \chi^2(\text{sol}) - \chi^2(\text{best}) \leq 1.0$, corresponding to 1σ in the case of one parameter of interest (Avni 1976).

In some cases we are not able to derive a measurement for the galaxy or the AGN components but we can still define a meaningful upper limit on the unconstrained component. In unobscured type-1 AGN, if the rest-frame K-band luminosity of the host galaxy is smaller than 10% of the AGN luminosity in the same rest-frame band, we assign an upper limit to the host galaxy SED component. This is the case for 34 type-1 AGN for which the value of the upper limit of the galaxy K-band luminosity is taken as the highest possible value of the parameter within the uncertainty. In these cases we assign an upper limit also to the object's total stellar mass assuming the median mass-to-light ratio of all other objects in the sample. No rest-frame magnitudes in U- and B-band are derived in these cases.

On the other hand, for 279 obscured type-2 AGN which are not detected in the $24\mu\text{m}$ Spitzer/MIPS band, we can provide only upper limits on the AGN component (and thus on the AGN luminosity). This is because in heavily obscured sources the AGN component rises almost exclusively at NIR wavelengths, and without

⁵ In fact, due to an insufficient photometric coverage, 5 sources have been excluded from the analysis, while for 18 sources no good solution could be found due to problems in the photometry or in the SED: the reduced χ^2 in these cases is large (>20). For these sources no physical parameters could be derived.

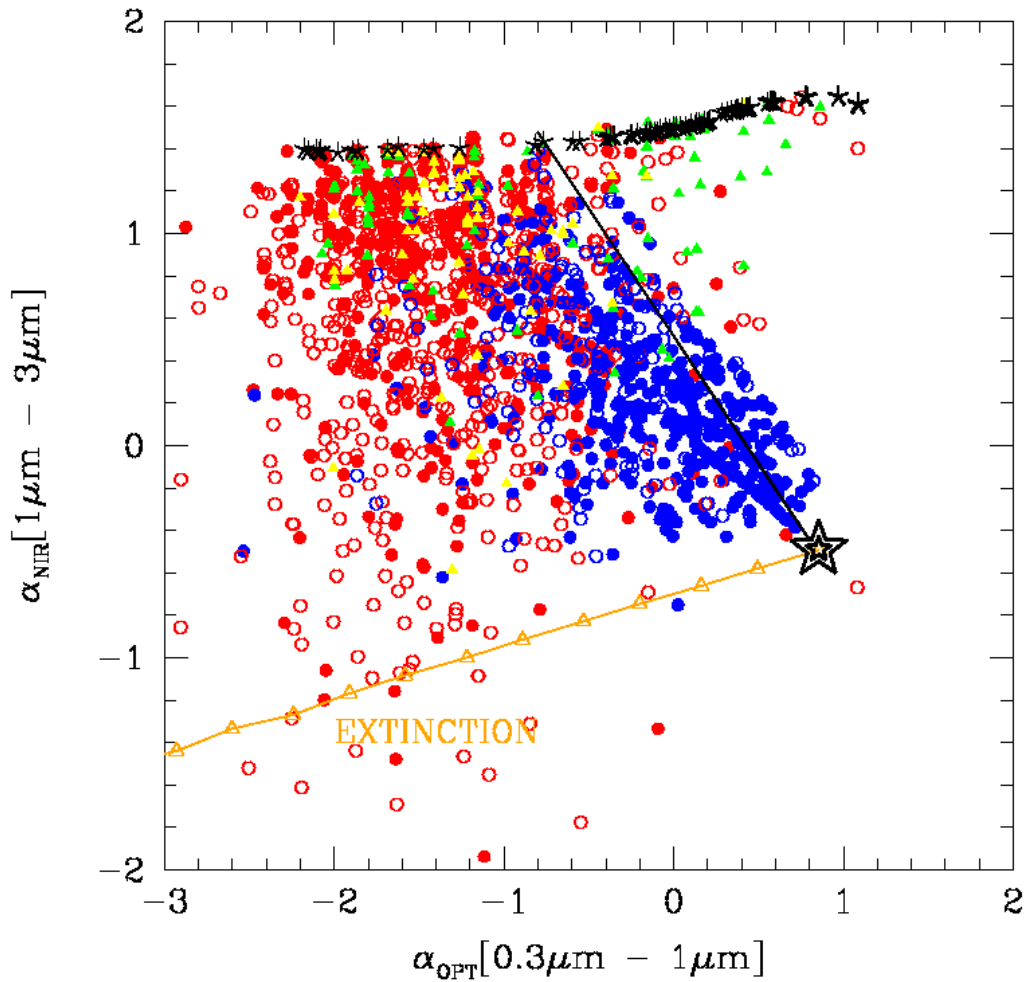


Figure 5. *Mixing Diagram from Hao et al. (2010):* slope - slope plot of the entire sample of analyzed AGN. Circles correspond to XMM-COSMOS obscured (red) and unobscured (blue) AGN; green and yellow triangles show the optically selected AGN (selected using the BPT diagram and the NeV line). Open and filled circles correspond to photometric and spectroscopic redshifts. The big star show the R06 mean SED while the asterisks show different BC03 galaxy templates. The black line indicates the boundaries of the possible slopes obtained by mixing the R06 template with different fractions (0% - 100%) of a given galaxy template. The orange line shows the reddening vector of R06 with the triangles corresponding to steps of 0.1 in E(B-V).

the $24\mu\text{m}$ detection it is not possible to determine reliably the AGN contribution to the optical/IR SED. For these sources, we derived an upper limit on the $12\mu\text{m}$ rest-frame AGN luminosity (see below) using the $24\mu\text{m}$ detection limit and applying the appropriate k -correction. We note here that in these cases, we can still use the observed X-ray (or emission line) luminosity to infer the level of AGN strength in the source.

Summarizing, from the initial sample of 1702 sources the SED fitting was successfully applied to 1679 sources. Of these objects, 34 type-1 AGN have only an upper limit in the galaxy component parameters (mass and rest-frame M_K) while no U- and B-band rest frame magnitudes were assigned. For 279 type-2 AGN only an upper limit in the AGN component parameters ($L_{12.3\mu\text{m}}$ and thus L_{bol}) could be derived. All the derived parameters are available online. An example of the published table can be found in Table C2.

3.4 AGN-galaxy Mixing Diagram

Based on our SED fitting procedure described in the previous section, Figure 5 shows the rest-frame NIR and optical slopes of the total best fit SED of the sources in our sample (adapted from Hao et al. 2010). For each source we plot the slopes on either side of the rest-frame $1\mu\text{m}$ which is approximately the inversion point in the typical QSO SED in a $\nu f(\nu)$ versus ν representation (i.e. where the exponent of a locally power-law fit to the SED changes sign). In particular, we computed the IR slope (α_{NIR}) between $1\mu\text{m}$ and $3\mu\text{m}$ and the optical slope (α_{OPT}) between $0.3\mu\text{m}$ and $1\mu\text{m}$ (for more details see Hao et al. 2010; Elvis et al. 2012). The location of the sources in this ‘color-color’ space is then shown in Fig. 5, where circles represent XMM-COSMOS obscured (red) and unobscured (blue) AGN, while triangles correspond to the optically selected sources without X-ray counterpart (green for AGN selected with the diagnostic diagrams and yellow for NeV selected AGN). Open and filled circles correspond to photometric and spectroscopic red-

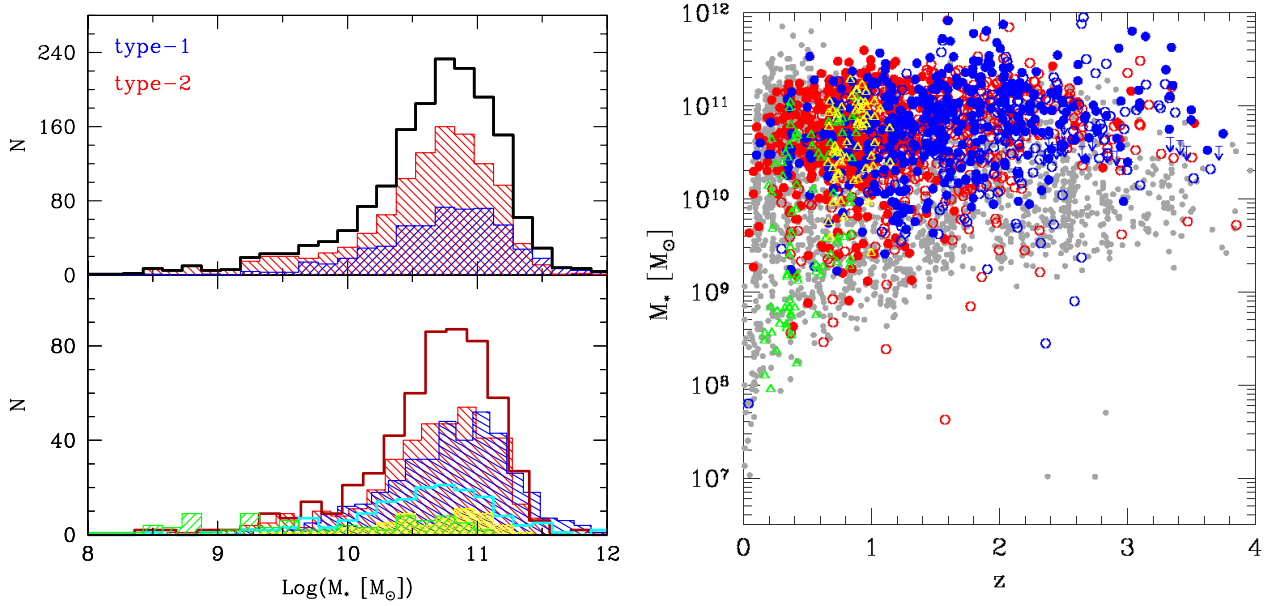


Figure 6. *Left:* In the lower panel we show the stellar mass distribution of the AGN host galaxies for the different analyzed sub-samples: shaded blue and red for spectroscopically confirmed X-ray type-1 and type-2 AGN, empty cyan and red for X-ray selected type-1 and type-2 AGN with photometric redshift, dashed green and yellow for optically selected through emission lines (green: BPT diagram and yellow: NeV line) without X-ray detection. The top panel shows instead the entire sample (thick open histogram) and divided in type-1 (shaded blue) and type-2 (shaded red) AGN. *Right:* Host galaxy stellar masses versus redshift for the entire AGN sample with the usual color-coded sub-classes division. We also show in gray the distribution of masses for the I-band-apparent-magnitude-matched parent galaxy population.

shift. Note that the same symbols and color-code is used throughout the paper.

In the plot, the big star indicates the SED of our pure type-1 AGN template, for which $\alpha_{\text{OPT}}=0.85$ and $\alpha_{\text{NIR}}=-0.49$ (Richards et al. 2006, hereafter R06). Starting from this point, the orange line shows the R06 template when reddening is applied (the orange triangles correspond to steps in $E(B-V)$ of 0.1). The asterisks show the position in this diagram of different galaxy templates derived from the stellar population synthesis models of Bruzual & Charlot (2003, hereafter BC03) adopted: from passive to extreme starbursts going from left to right. The black line indicates the R06 template when mixed with different fractions (0% - 100%) of a given galaxy template. This mixing curve defines the boundaries of the possible slopes obtained by mixing the R06 with this particular galaxy template. This plot shows the three main components of the typical SED of the analyzed sources (AGN, host galaxy and extinction) and their relative contributions to the total SED and serves as a powerful illustration of the level of “contamination” of the optical/IR SED of AGN, at least at the luminosity levels probed by the COSMOS survey. As visible in figure, for type-1 unobscured AGN the galaxy contamination is less predominant than in type-2 obscured AGN, where high value of extinction are associated to high contamination of the host galaxy which can dominate in the $0.3\mu\text{m} - 3\mu\text{m}$ interval. Moreover, there are no objects along the AGN extinct line at $E(B-V)>1$ showing that when the AGN absorption is high, the galaxy contribution becomes important.

Most of the sources lie on the left-side region of the $\alpha_{\text{OPT}}-\alpha_{\text{NIR}}$ plot, and only a small percentage (and only obscured AGN) lie in the upper right corner. This is a consequence of the fact that in nature galaxies with high star formation rates typically show high levels of obscuration, too. This means that, while we do include

non-extinct starburst templates in our library, these solutions are almost never chosen because unrealistic (unless t_{age} or τ/t_{age} are very low, as is the case for the few points in that region of the plot).

Unobscured AGN in this region of the plot have been interpreted by Hao et al. (2010) as hot-dust-poor (HDP) quasars i.e. normal quasar with a relatively weak IR bump. However, for the obscured ones, another possible explanation is that these sources are normal AGN hosted by starburst galaxies which steepen the UV slope. Looking one by one at the SED of all these sources we found that all but four of them are not detected at $24\mu\text{m}$ and their SED in the UV-optical part is dominated by a starburst galaxy. Most of these sources are Seyfert-2 galaxies optically selected using BPT diagrams. Some of them, due to the errors associated to the line measurements, can be misclassified normal star forming galaxies. Alternatively they could be very faint AGN hosted in starburst galaxies.

3.5 Measuring AGN host stellar masses and star formation rates

3.5.1 Stellar masses

The SED fitting procedure allows us to estimate the total stellar mass and the star formation rate (SFR) of the AGN host galaxies. Knowing the IMF, for a given star-formation history, each combination of τ and t_{age} (see Sec. 3.1) is in fact uniquely associated to a value of specific star formation rate (sSFR=SFR/M, see Sec. 4.4) and, given the normalization of the template, total stellar mass.

For our AGN COSMOS sample, we have thus derived a robust estimate of the host galaxy stellar masses for 1650 objects (out of a total number of 1702 attempted SED fits). As explained in Sec. 3.1, for 34 type-1 AGN we could derive only an upper limit on the

stellar mass, while for 18 objects the SED fit failed due to problems in the photometry or in the SED shape, so no mass estimation was possible.

The top left panel of figure 6 shows the host galaxies stellar mass distribution for the entire AGN sample (open histogram) and divided in type-1 (hatched blue) and type-2 (hatched red) objects. The bottom panel shows a detail of the M_* distribution in the different sub-samples, color-coded as usual. Masses range mainly from $10^{10}M_{\odot}$ to $10^{11.5}M_{\odot}$ with a peak at $10^{10.9}M_{\odot}$. No significant difference is found between the type-1 and type-2 AGN host population which show on average the same host galaxy mass distribution. Interestingly, the hosts of optically selected Seyfert-2 galaxies without X-ray counterpart show a tail in the distribution at lower masses down to $10^{8.5}M_{\odot}$.

The right panel of Fig. 6 shows instead the stellar masses of the AGN hosts as a function of redshift superimposed on the underlying distribution of stellar masses of non-AGN in the COSMOS area drawn from Ilbert et al. (2010) and matched to the AGN population in redshift and I-band apparent magnitude (see Sec. 2.4).

3.5.2 Star formation rate

The measure of the host galaxy SFR is subject to considerably larger uncertainties than that of stellar mass, in particular for type-1 AGN. In general, the most reliable way to compute the SFR is summing up the rate of unobscured star formation (emitted in the UV) with the obscured one re-emitted in the (mid- and far-) IR by dust (SFR_{UV+IR}). Our optical/IR SED fitting procedure relies only on the UV emission measurements, which traces only the unobscured SF, which is however scaled up by the dust correction factor computed using the full SED to account for the latter contribution.

The issue of the reliability of UV-based indicators of star formation rates in galaxies is a long-standing one. With the advent of the *Herschel* telescope, sensitive Far-IR measurements of cold dust heated by star-forming processes has become available for deep and medium-deep surveys of the extragalactic sky, providing a first direct handle of SFR_{UV+IR} in large samples of galaxies (see e.g. Rodighiero et al. 2010). For complete samples of AGN selected in both X-rays and optical spectroscopic surveys, however, the final answer to the question of what are the intrinsic star-forming properties of the AGN hosts requires SFR indicators that are sensitive to both star-forming galaxies and passive/quiescent ones. This is not possible even for *Herschel*, whose sensitivity to individual galaxies does not reach into the quiescent population at the redshifts ($z > 1$) of deep extragalactic surveys such as COSMOS (see e.g. Shao et al. 2010; Mullaney et al. 2012). Indeed, only $\sim 10\%$ of the AGN in our sample are detected above the 3σ limits of the PEP catalogues in the COSMOS field. In Appendix B we compare the SFR estimated from the SED fitting with the one derived with other methods (i.e. FIR observation and optical emission lines). We find that above $\sim 20 M_{\odot} \text{ yr}^{-1}$ the agreement between the SFR derived from the SED and the one derived from the FIR bands is quite good, while at lower SFR ($< 20 M_{\odot} \text{ yr}^{-1}$) the disagreement becomes evident, with SFR(FIR) being systematically higher than SFR(SED). We interpreted this discrepancy as a combination of a possible contamination from SF in the NIR not properly taken into account in the SED fitting together with a not-negligible AGN contamination to the FIR bands not taken into account in the FIR SFR estimates (see e.g. Rosario et al. 2012). This would imply that, while our SFR estimates can be in some cases underestimated, the FIR-SFR can be overestimated especially at lower SFR where the AGN contamination would represent a significant fraction of the IR emission.

In any case, the very nature of our objects, and the SED decomposition technique with which we analyze them, require some special care in the interpretation of the SFR measurements. The main problem with type-1 (unobscured) AGN is that the accretion disk emission strongly contributes in the UV band (see upper panels of Fig. 3) introducing a degeneracy in the SED fitting between the UV emission from star formation and from the central AGN. In practical terms this means that, in some cases the SED fitting can give two significantly different solutions with a similar χ^2 : an unobscured AGN, with a prominent Big Blue Bump (BBB) dominating in the UV range with a passive/moderately star forming galaxy or, conversely, a moderately obscured AGN with a strongly star-forming galaxy, which substantially contributes to the observed UV emission. Since it is not possible to disentangle *a priori* this kind of degeneracy, we will not take into consideration the SFR measurements of type-1 AGN for the further discussion.

On the contrary, since in obscured AGN the UV emission is suppressed by obscuration (see, as an example, the bottom panels of Fig. 3), the UV range is clean from AGN contamination and a reliable estimate of the SFR can be derived from the SED.

Figure 7 shows the host galaxy SFR distribution in three redshift bins for 1090 obscured type-2 AGN (thick solid line) and for the different sub-samples with the usual color code. AGN host galaxies span a very wide range of SFR, with X-ray selected AGN populating the entire range, while optically selected Seyfert-2 galaxies (which are mainly at low redshifts) are hosted predominantly in galaxies with low SFR (but very low masses as shown in Fig. 6). This can highlight a physical difference in the hosts of optically selected Seyfert-2 galaxies or can be, at least partly, driven by the fact that high SFR implies strong emission line dilution which causes a certain fraction of AGN to be missed by the emission line ratios (BPT) selection.

3.6 Measuring nuclear $L_{12\mu\text{m}}$ and bolometric luminosities

Before proceeding to a comprehensive discussion of the observable (and physical) properties of the host galaxies of the AGN selected in COSMOS, we present some basic “intrinsic” properties of the AGN population itself. This will be also a useful reminder that, in terms of the physical characteristics of growing black holes and of their immediate (nuclear) environments, every large survey selects families of objects occupying specific parts of the generic parameter space identified by the distance of the source, its accretion luminosity, BH mass, and level of nuclear obscuration.

To begin with, we note that from the best fitting (obscured or un-obscured) AGN component in the SED, we can derive an estimate of the AGN luminosity at (rest-frame) $12\mu\text{m}$ which can be used as a reliable estimator of the AGN bolometric luminosity. The intrinsic AGN $12\mu\text{m}$ luminosity is calculated by integrating the AGN component obtained from the best SED fit over a narrow (i.e., $1\mu\text{m}$) pass-band centered on $12\mu\text{m}$. By construction, and given the shape of the BC03 templates used to fit the galaxy component in every system, the mid-IR band is assumed to be completely dominated by the nuclear AGN light reprocessed in the obscuring molecular structure on $\sim 1 - 10$ pc scale. Such a drastic assumption is likely not to be correct for a number of individual objects, which may have a significant galaxy contribution (not included in BC03 templates) at $12\mu\text{m}$. However, globally it is not unreasonable for the studied AGN sample as suggested in Fig. 8, where the AGN $12\mu\text{m}$ luminosity is plotted against the intrinsic (de-absorbed) X-

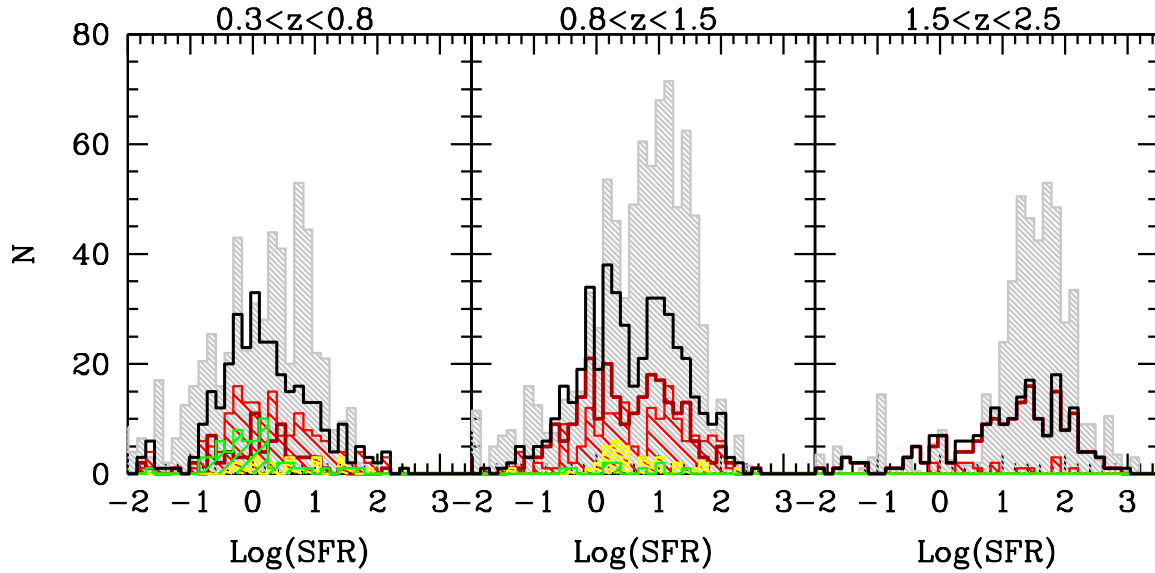


Figure 7. Star formation rate distributions in three redshift bins of the AGN host galaxies for the entire type-2 AGN sample (thick open histogram) and divided in different sub-samples: shadow and empty red for X-ray spectroscopically confirmed and with only photometric redshift type-2 AGN, dashed green and yellow for optically selected through emission lines (green: BPT diagram and yellow: NeV line) without X-ray detection. The gray histogram shows as comparison the distribution of the mass-matched parent sample. To make easier the comparison, the latter has been divided by a factor of two.

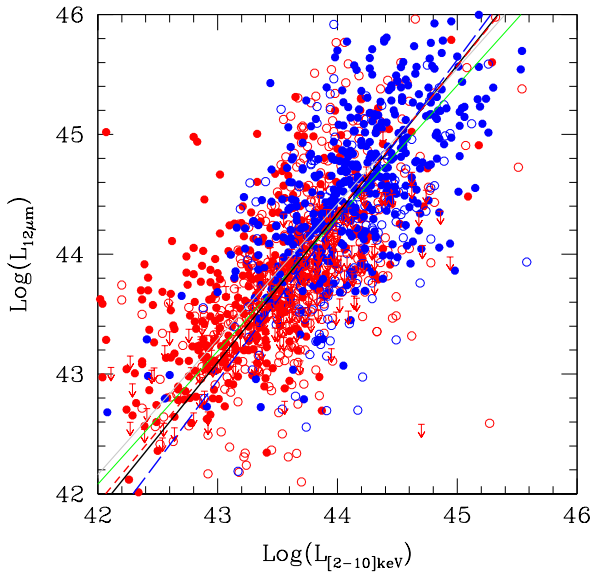


Figure 8. X-ray [2-10] keV versus mid-infrared $12\mu\text{m}$ luminosities for the sample of ~ 1550 AGN with X-ray detection and measured $L_{12\mu\text{m}}$. Red circles are spectroscopic (filled) and photometric (open) type-2 AGN while type-1 AGN are represented with filled (spectroscopic) and open (photometric) blue circles. The thin solid green diagonal line is the [2-10]keV - $12.3\mu\text{m}$ luminosity relation found by Gandhi et al. (2009) for the sample of 22 well resolved local Seyfert. The thick solid lines are the fitted correlation considering our entire sample (black) and only the spectroscopic sources (gray), while the long-dashed blue and the short-dashed red correspond to the type-1 and type-2 sub-sample.

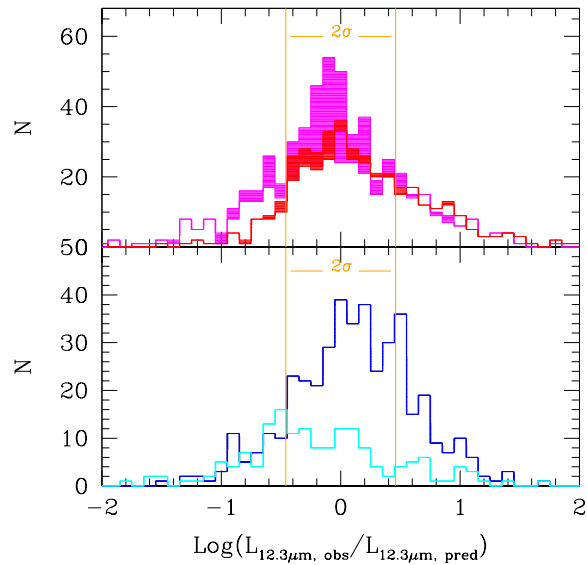


Figure 9. Histograms of the ratio between the measured $12.3\mu\text{m}$ luminosity and the one predicted by the Gandhi et al. (2009) relation on the basis of the observed 2-10 keV X-ray luminosity. In the top panel we show type-2 AGN, with the red histogram marking objects in the spectroscopic sample and the purple one those with photometric redshifts; filled histograms are for upper limits. In the bottom panel we show instead the type-1 AGN, with the dark histogram marking objects in the spectroscopic sample and the cyan one those with photometric redshifts. Yellow histograms in both panels show the outliers in the mixing diagram of Fig. 5 (see text for more details). The two solid orange lines delimit 2σ from the Gandhi relation (mean equal to zero and standard deviation $\sigma=0.23$).

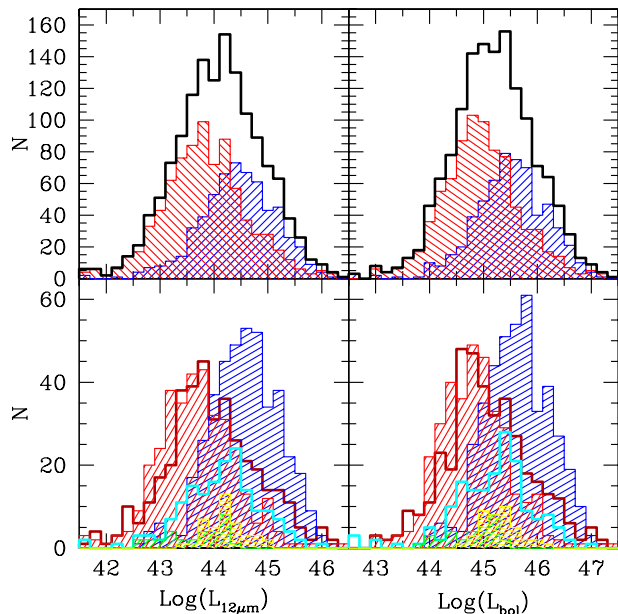


Figure 10. *Upper Panels:* Mid-IR and bolometric luminosity distribution of the entire sample (thick open histogram) and for the type-1 (shaded blue) and type-2 (shaded red) AGN sub-samples separately. *Bottom Panels:* Mid-IR and bolometric luminosity distribution of the different sub-samples included in our AGN sample: shaded blue and red for X-ray spectroscopically confirmed type-1 and type-2 AGN, empty cyan and red for X-ray selected type-1 and type-2 AGN with photometric redshifts, dashed green and yellow for optically selected through emission lines (green: BPT diagram and yellow: NeV line) without X-ray detection.

ray [2-10] keV luminosity⁶ for the XMM selected sample of ~ 1550 objects with X-ray detections and $L_{12\mu\text{m}}$ measurements.

Using a sample of local Seyfert galaxies (both Seyfert-1 and Seyfert-2) at high spatial resolution, Gandhi et al. (2009) found that the uncontaminated nuclear mid-IR continuum of AGN closely correlates with the X-ray [2-10] keV AGN emitted powers over three orders of magnitude in luminosity. To be specific, the best-fit correlation they obtained considering only the 22 well-resolved sources is shown as a thin green line in Fig. 8 ($\text{Log}(L_{\text{MIR}}/10^{43}) = (0.19 \pm 0.05) + (1.11 \pm 0.07)\text{Log}(L_X/10^{43})$). Our data follow the Gandhi’s relation. As a comparison, the fit to our data performed adopting the ordinary least-square bisector estimate recommended by Isobe et al. (1990), which gives identical weighting to all sources, gives $\text{Log}(L_{\text{MIR}}/10^{43}) = (0.10 \pm 0.03) + (1.24 \pm 0.03)\text{Log}(L_X/10^{43})$ for the entire sample and $\text{Log}(L_{\text{MIR}}/10^{43}) = (0.29 \pm 0.03) + (1.13 \pm 0.03)\text{Log}(L_X/10^{43})$ if we consider only the spectroscopic sample. The fits are shown respectively as black and gray solid thick lines in Fig. 8, together with the fit for the type-1 (blue long-dashed line) and type-2 (red short-dashed) AGN sub-samples. The good agreement between the predicted and the measured $12.3\mu\text{m}$ luminosities is also shown in Fig. 9 where we show the histogram of the ratio between the measured $12.3\mu\text{m}$ luminosity and the one predicted by the Gandhi et al. (2009) relation for type2 (top panel) and type1 AGN (bottom panel). We notice that, while the distribution of the

ratio between the measured and the predicted MIR luminosity is centered at zero⁷, the observed scatter is much larger than the one measured by Gandhi et al. (2009) (2σ from the Gandhi relation is delimited with orange lines: mean equal to zero and standard deviation $\sigma=0.23$). If we consider only the sources with a spectroscopic redshift (black solid line), we do see a clear asymmetry in the distributions, as expected due to the un-accounted contribution of star-formation-related emission in the NIR (see also Lusso et al. 2011). Indeed, while $\sim 61\%$ of the objects are found within 2σ of the distribution, the tail extending to lower values includes 94 sources (12%), while for a higher number of sources (211, 27% of the sample) the observed mid-infrared luminosities are significantly higher than the predicted ones. This is however not the case for the photometric sample. A possible explanation of this effect might involve the effect of the uncertainties in the photometric classification in some of the AGN for which we miss spectroscopic information. Indeed, we have tested that all the small fraction of outliers in the diagram of Fig. 5 (i.e. type-1 AGN with $\alpha_{\text{OPT}} < -1$ and type-2 AGN with $\alpha_{\text{OPT}} > -1$), show a broader distribution in the $L_{12.3\mu\text{m,obs}}/L_{12.3\mu\text{m,pred}}$ ratio with a slight skew towards values less than unity.

Part of the observed differences can also be attributed to the fact that we are extending the Gandhi relation, which was derived for a sample of local Seyfert galaxies, to a sample spanning a much wider luminosity and redshift range. However, it is also plausible that in a fraction of these sources the SED-fitting procedure overestimates the nuclear contribution resulting in a higher $L_{12.3\mu\text{m,obs}}$ compared to the predicted $L_{12.3\mu\text{m,pred}}$. How much of this scatter is inherently due to the physical conditions of the AGN and torus clouds, as compared to observational selection effects, remains an important unresolved issue, which is beyond the scope of this paper. However, the comparison points out that on average the $12.3\mu\text{m}$ luminosity derived from the SED fitting is a reasonably good measure of the mid-IR AGN luminosity and that indeed the assumption that the mid-IR emission is dominated by the AGN emission due to accretion onto the central black hole rather than SF from the host galaxy is plausible for most of the sources.

One clear advantage of adopting the rest-frame MIR luminosity, $L_{12\mu\text{m}}$, as a universal AGN power estimator for our sample is that, contrary to the [2-10] keV luminosity, this quantity was measured homogeneously for all the sources, including the objects with no X-ray emission. Hence it can be used to compare the AGN power in the different sub-samples and to derive in a homogeneous way the bolometric luminosity for the entire sample⁸. This is shown in Fig. 10 where both the $12\mu\text{m}$ and the derived bolometric luminosity using the Hopkins et al. (2007) conversions are shown for the different sub-samples (bottom panels) and for the full sample divided in obscured and unobscured AGN (upper panels). Bolometric luminosities range from 10^{43} to 10^{47} erg s⁻¹.

Optically selected Seyfert-2 galaxies (green histogram) are among the faintest sources in our sample extending down to $L_{\text{bol}}=10^{43}$ erg s⁻¹. Since their $12\mu\text{m}$ luminosities are of the same order of the X-ray selected obscured sources, the lack of X-ray detection can be due to the fact that these sources lie in the tail of the Gandhi relation (Fig. 9). Alternatively, some of these sources

⁶ Calculated on the basis of the observed fluxes in the soft (0.5-2 keV) and hard (2-10 keV) X-ray energy bands, of the known redshift, and assuming, as X-ray spectral model, an intrinsic power-law of slope $\Gamma = 1.9 \pm 0.2$, absorbed by neutral gas.

⁷ in contrast to Lusso et al. (2011) which found a shift of 0.2 towards higher values when considering the ratio between the total (AGN+GAL) SED and the Gandhi predicted values.

⁸ However, for a more detailed study of the bolometric luminosities of XMM-COSMOS AGN we refer the reader to Lusso et al. (2010, 2011).

can be Compton-thick AGN, as shown by Gilli et al. (2010) for the [Ne v]-based sample, and, due to the high N_{H} absorption, they are not detected in the X-ray band.

4 THE PHYSICAL PROPERTIES OF COSMOS AGN HOST GALAXIES

4.1 Rest frame colors

The unique strength of the COSMOS AGN sample at hand, lies indeed with the possibility, by means of our SED fitting technique, of reliably removing the AGN component from the overall SED of any AGN host. In this section, we thus discuss rest-frame observables (absolute magnitudes and colors) of the AGN host galaxy component, which are, by construction, little contaminated by the AGN colors. We also investigate the properties of the AGN host galaxies compared to normal galaxies.

Figure 11 shows the rest frame U–B colors versus the B-band absolute magnitude (the color-magnitude diagram, CMD) for our sample of AGN hosts divided in three different redshift bins ($[0.3 < z \leq 0.8]$, $[0.8 < z \leq 1.5]$ and $[1.5 < z \leq 2.5]$). The gray contours show for comparison the whole galaxy sample drawn from Ilbert et al. (2010) in the same redshift intervals, while grey points correspond to the mass-matched parent sample described in Sec. 2.4. We have chosen to show both the ‘measured’ values of the U–B colors (upper row) and the extinction corrected ones, where the value of the extinction is that obtained for the galaxy component from the best fit SED decomposition (see section 3.2.1). This is an important test, as galaxies with red colors can be either dusty star-forming galaxies or galaxies with old stellar populations, and any interpretation of the location of AGN hosts in the CMD may be strongly affected by the treatment of dust extinction in these systems (see e.g. Cardamone et al. 2010). Our rich and comprehensive multi-wavelength dataset is very well suited to attempt a robust determination of the large scale extinction properties of the galaxies in the various samples.

First of all, a note of caution is in place, as, at any given host galaxy magnitude, the colors of the type–1 hosts are more and more unreliable the higher the nuclear AGN luminosity. In this respect, very blue colors of bright type–1 AGN (see, in particular, the clusters of sources at $U-B \approx 0.1-0.3$ in all extinction corrected CMD) should not be too trustworthy, as they most likely indicate objects for which the SED decomposition, and thus the AGN blue light subtraction, may give uncertain and possibly unreliable results. We will come back to this point when discussing the inferred star formation rate properties of the AGN hosts.

We now move to the discussion of the CMD of the general AGN hosts population. Underneath each of the diagrams, Fig. 11 shows the fraction of all AGN (black), type–1 AGN (blue) and type–2 AGN (red) relatively to the whole galaxy population in the corresponding redshift bin as a function of B-band magnitude. For consistency, in the computation of these fractions we restrict the analysis to the X-ray detected sample, the completeness of which can be properly assessed in a relatively simple way (see e.g. Sec. 4.3 below), noticing however that the only effect of the pure optical sources is to slightly flatten the slope at lower redshifts. In agreement with previous studies (Nandra et al. 2007; Brusa et al. 2009b), the AGN are almost exclusively hosted in bright ($M_{\text{B}} < -20$) galaxies and the fraction of galaxies hosting AGN increases going to higher luminosities.

No significant difference is found in the host’s colors of

unobscured and obscured AGN, in contrast with what expected from the most popular models of AGN fueling and feedback (e.g. Hopkins et al. 2008) but in agreement with the standard unified model (Antonucci 1993). As a matter of fact, the relative fraction of type–1 and type–2 AGN changes only slightly with B-band luminosity in each redshift interval, but the overall fractions of obscured and unobscured AGN are markedly different in the three redshift bins. This is an effect introduced by the well known anti-correlation between obscured AGN fraction and luminosity (see e.g. Hasinger 2008) in combination with the almost constant (X-ray) flux limit of the XMM-COSMOS survey, which implies that high redshift sources are more luminous than low redshift ones. A comprehensive discussion of the incidence of obscured and un-obscured AGN in the COSMOS field as a function of luminosity, redshift and host galaxy properties will be presented in a separate work (Merloni et al. in prep.).

We find no evidence of color bi-modality for AGN hosts, which populates mainly the red and intermediate part of the bimodal color magnitude distribution observed for normal galaxies. Interestingly, at $0.3 < z < 0.8$ the low luminosity, optically selected (from BPT diagram) Seyfert–2 galaxies without X-ray counterpart (green triangles) seem to behave in a different way, being mainly hosted in galaxies populating the blue and the intermediate region. The effects of dust extinction correction on the AGN distribution in the color-magnitude diagram are clearly visible in the lower panels of Fig. 11, where some objects populating the red sequence moved to the intermediate $U-B$ region and some that were in the intermediate region lie now in the blue region (see also Cardamone et al. 2010). However, in contrast to what was found by Cardamone et al. (2010), no clear bi-modality is seen in any of the three panels even after dust correction is applied. More importantly, it is clear from Fig. 11 that dust extinction correction affects more severely the overall color distribution of the parent galaxy sample. This can be seen in the fact that the AGN fraction in the B-band most luminous galaxies in the sample decreases once dust correction is included.

Indeed, at any redshift, AGN hosts are found mainly in red galaxies, albeit with a substantial tail towards intermediate and bluer colors (see also Fig. 12). In many previous studies, AGN were described as populating preferentially an intermediate region, the so called “green valley” (Silverman et al. 2009), with the possible interpretation that they live in quenched galaxies going through the transition phase between active and passive star-formation phase. However, most of these works were focused on small subsample of the AGN population and, more important, the AGN component was not subtracted in the computation of the host colors leading to a possible blue contamination from the AGN which in fact would push red hosts into the green valley. Moreover, the net effect of the dust correction applied systematically, and in a uniform way, to both the parent and the AGN host galaxy samples is to *decrease* the fraction of AGN in the most star-forming objects.

In general, the often contrasting interpretations of many previous studies of the CMD of AGN hosts from deep multi-wavelength surveys (Nandra et al. 2007; Silverman et al. 2009; Xue et al. 2010; Cardamone et al. 2010; Rosario et al. 2011) demonstrates that studying their position within optical color-magnitude diagrams is hardly a robust way to unveil the star-forming nature of AGN hosts. This is because the interpretation of optical colors in terms of star-formation properties of a galaxy can suffer from various, degenerate, biases, especially when dealing with distant AGN hosts. To counter such degeneracies, at least partly, in section 4.4 we will discuss in more detail how AGN hosts are distributed in the physical parameter space of stellar mass and star formation rate.

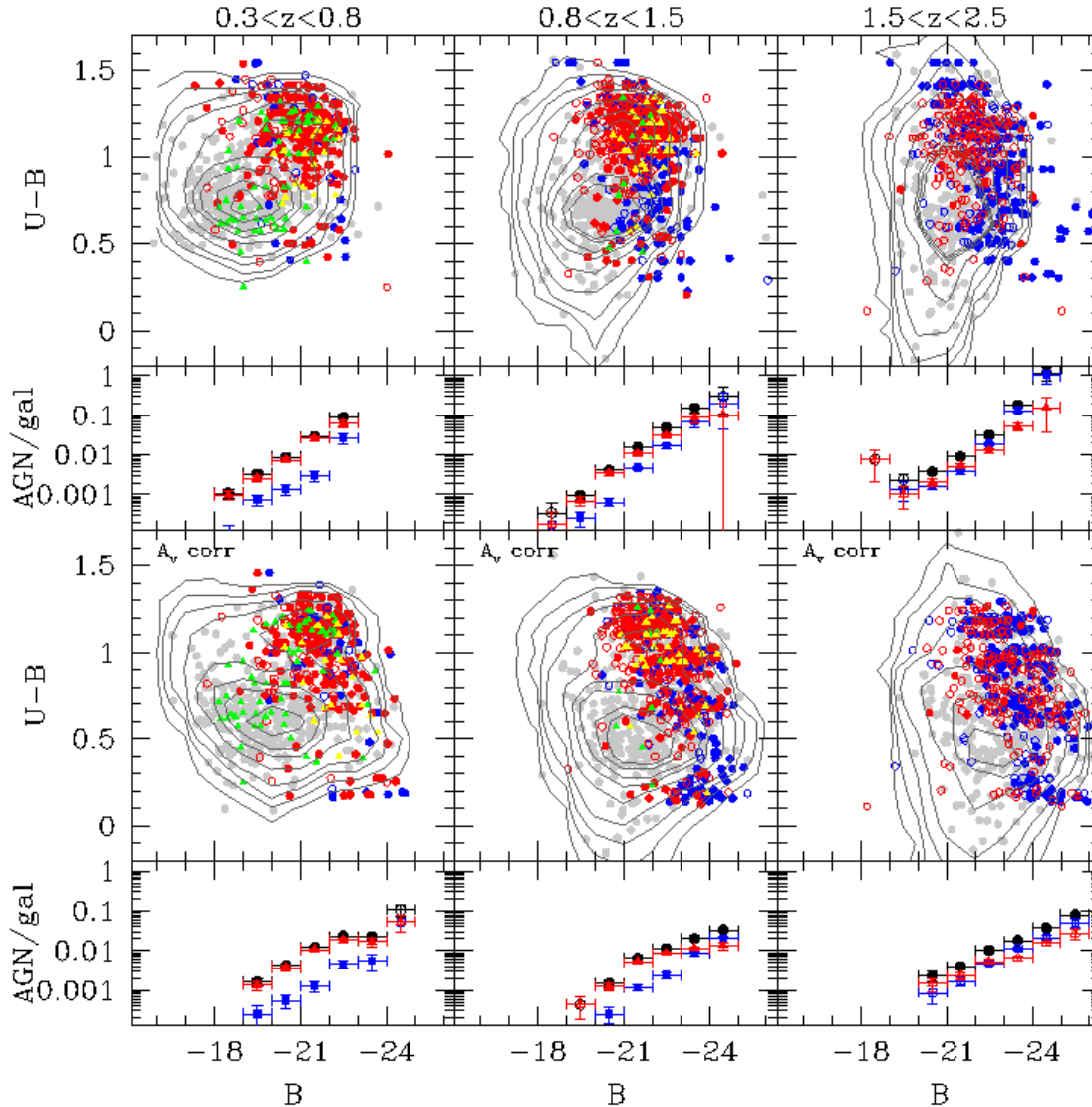


Figure 11. *Upper Panels:* $U-B$ vs M_B color-magnitude-diagram AGN host galaxies of unobscured (blue circles) and obscured (red circle) X-ray AGN and optically selected (green and yellow triangles) AGN in three redshift bins. Open and filled circles correspond to photometric and spectroscopic redshift. Grey contours show the whole galaxy sample drawn from Ilbert et al. (2010) while grey points correspond to the mass-matched parent sample described in Sec. 2.4. *Lower Panels:* Same as above but now M_B and $U-B$ are de-reddened using the $E(B-V)$ derived from the SED fit. The bottom part of each panel shows the fraction of galaxies with an AGN as a function of B magnitude, considering all AGN (black circles), only type-1 (blue squares) and only type-2 (red triangles) AGN. For these fractions, we consider only X-ray selected AGN and the whole galaxy sample.

4.2 Host galaxy color-mass diagrams

Figure 12 shows the position of our AGN sources in the color-mass diagram, where the colors ($U-V$) are corrected for extinction. Black contours show the whole galaxy sample drawn from Ilbert et al. (2010) while grey points correspond to the i -band-apparent-magnitude-matched parent sample described in Sec. 2.4. Comparing with the whole galaxy population, we find that, at any redshift, AGN are preferentially detected in massive galaxies, in agreement with previous studies (Brusa et al. 2009b; Silverman et al. 2009; Xue et al. 2010; Mullaney et al. 2012). The trend is still present if we use as comparison sample the i -band-matched sample. In the next section we will investigate in greater detail the evolution of

the AGN fraction as a function of redshift, X-ray luminosity, stellar mass of the host, and of the ratio of these two latter quantities. Here we note, however, that except for few unobscured AGN in the intermediate z bin showing extreme (and probably unreliable) blue colors, obscured and unobscured AGN overlap very well in the color-mass plane.

Since massive hosts tend to be redder, the trend with mass and the one with colors seen in the previous section should go in parallel. In many previous studies it has been pointed out how, removing the mass dependency i.e. using a mass-matched control sample, the trend with color disappears (Silverman et al. 2009; Xue et al. 2010; Mainieri et al. 2011; Rosario et al. 2011). However, this is

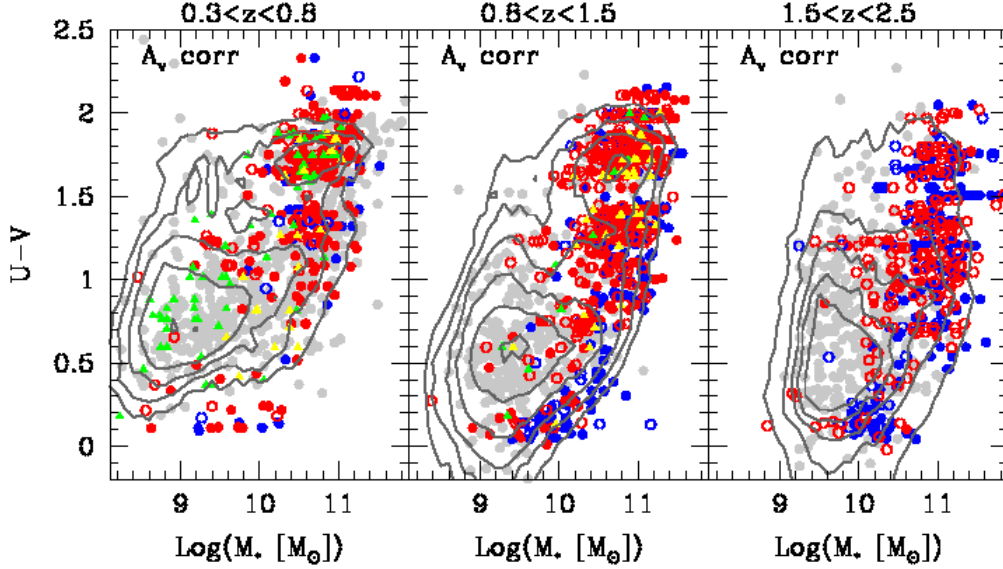


Figure 12. Extinction corrected color ($U-V$) vs mass diagram of AGN host galaxies of unobscured (blue circles) and obscured (red circle) X-ray AGN and optically selected (green and yellow triangles) AGN in three redshift bins. Open and filled circles correspond to photometric and spectroscopic redshift. Grey contours show the whole galaxy sample drawn from Ilbert et al. (2010) while grey points correspond to the i -band-apparent-magnitude-matched parent sample described in Sec. 2.4.

not the case in our study. Fig 13 shows the extinction corrected $U-B$ color histogram for AGN hosts in the usual three redshift bins, for three different ranges of stellar masses, all above the completeness threshold of the Ilbert et al. (2010) parent galaxy sample, divided into unobscured (shaded blue) and obscured (shaded red) AGN and compared to the mass-matched galaxy sample. Galaxies hosting an AGN tend to be redder than normal galaxies of comparable stellar mass (the median color shift ranges between ~ 0.1 and ~ 0.25).

Following our discussion in the previous section, we can speculate about two main reasons for the discrepancy between our color distributions of AGN hosts in mass-matched samples and previous studies. First of all, our SED decomposition technique allow a more reliable correction for AGN light “pollution” that would typically move the color of an AGN host towards the blue, star-forming sequence. Second, thanks to the unique multi-wavelength coverage of the COSMOS field, we are able to extinction-correct, in a systematic way, all galaxy colors, both in the parent and in the AGN host samples. We find that moving dusty star-forming galaxies back to the blue cloud with such a correction effectively decreases the incidence of AGN among star-forming galaxy, while, conversely, the relative fraction of AGN hosts in truly passive galaxies is enhanced. We caution however that, being these color shifts relatively small, systematic effects due to a non-optimal AGN-galaxy decomposition (AGN over-subtraction, see section 3.3) or to the specific choice of stellar population templates, could still be held responsible for some of this observed trend.

4.3 The incidence of AGN as a function of the host galaxies’ stellar masses

Let us now move to a quantitative assessment of the fraction of AGN as a function of host stellar mass. In order to do so, we need to take carefully into account the selection function of our survey. For this reason, in this section, we will consider only the X-ray selected

AGN, taking advantage from the well defined exposure map of the XMM-COSMOS survey (Cappelluti et al. 2009).

So far, one of the clearest pieces of evidence emerging from a variety of comparative studies of AGN and host galaxies in large multi-wavelength surveys is the fact that the likelihood of finding an AGN is a very strong function of the galaxy stellar mass, with AGN fractions (or, equivalently, duty cycles) increasing with increasing host galaxy stellar mass. This is a particularly strong effect for radio-selected AGN (Best et al. 2005; Smolčić 2009), but has been confirmed also for X-ray selected AGN (Brusa et al. 2009b; Xue et al. 2010; Mullaney et al. 2012).

4.3.1 AGN fraction as a function of X-ray luminosity

First of all, we compute the probability to find an AGN within a logarithmic bin of a given X-ray (2-10 keV, absorption corrected) luminosity, L_X , in different bins of stellar mass by taking the ratio of the number of AGN with measured host’s stellar mass in that range divided by the number of galaxies (of all morphological, color and star-formation activity types) having stellar mass in the same range in the parent sample of Ilbert et al. (2010):

$$p_{\text{AGN}}(L_X|M_*, z) = \frac{dN_{\text{AGN}}(z)}{d\log M_* d\log L_X} \frac{d\log M_*}{dN_{\text{gal}}(z)} \quad (6)$$

In practice, the sensitivity limits of the XMM-Newton observations vary spatially across the field (see Fig. 5 of Cappelluti et al. 2009), hence to derive the fraction of galaxies hosting an AGN as a function of the stellar mass, we followed the technique discussed in Sec. 3.1 of Lehmer et al. 2007 (see also Mainieri et al. 2011). The $p_{\text{AGN}}(L_X|M_*, z)$ for each stellar mass and luminosity bin is determined by the following equation:

$$p_{\text{AGN}}(L_X|M_*, z) = \frac{dN_{\text{AGN}}(L_X|M_*, z)}{d\bar{N}_{\text{gal}}(M_*, z) d\log L_X} \quad (7)$$

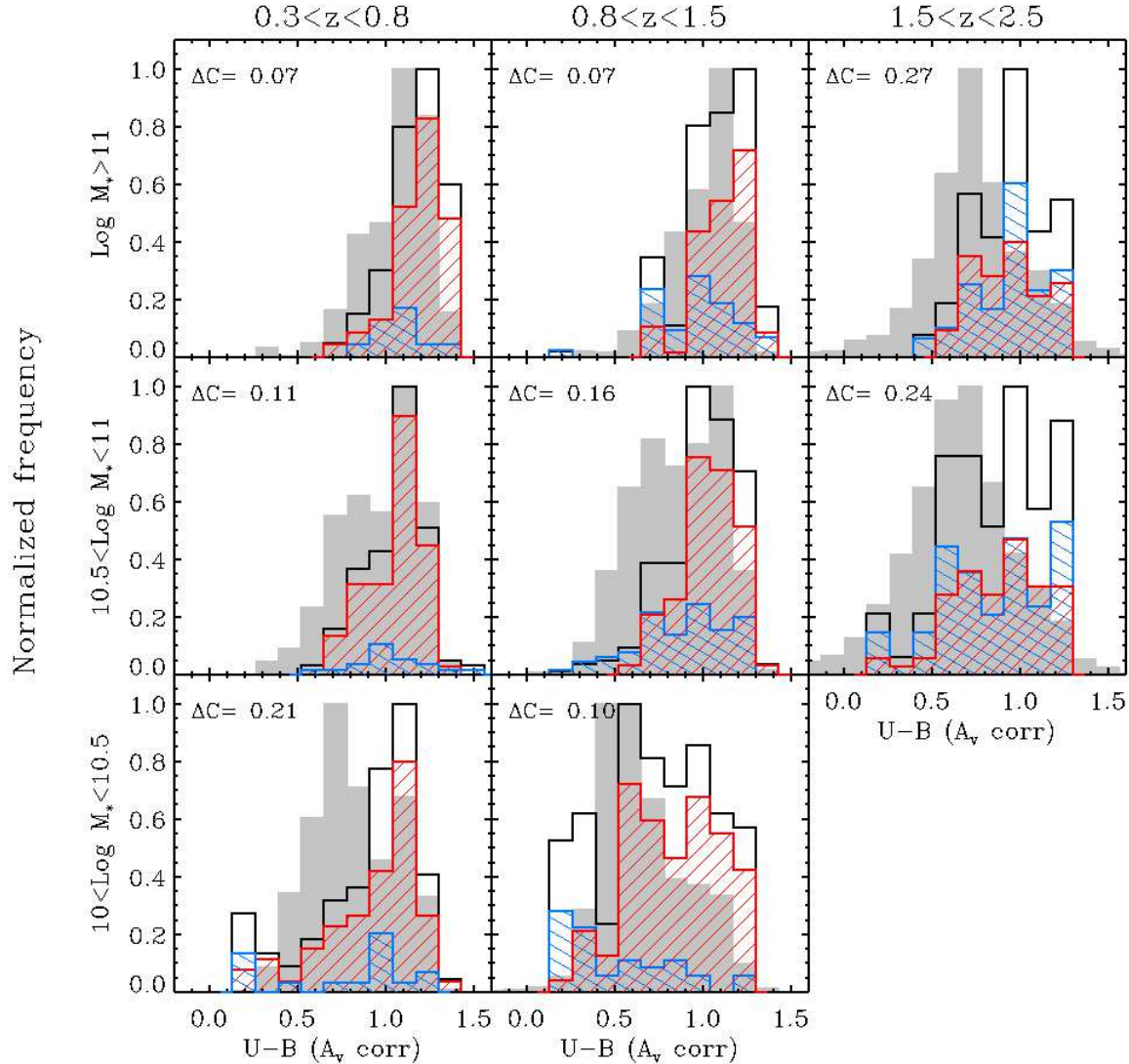


Figure 13. Rest frame extinction-corrected U–B color (normalized) distribution of AGN host galaxies in three redshift (from left to right) and mass (from bottom to top) bins. The black solid line corresponds to the total sample which is further divided into unobscured (blue shaded histogram) and obscured (red shaded histogram) AGN while the filled gray histogram corresponds to the galaxy sample. For each redshift interval we have considered only masses above which the parent sample is complete in stellar mass for both passive and star forming galaxies (Ilbert et al. 2010). In each panel the median shift in color $\Delta C \equiv \langle (U - B)_{\text{AGN}} \rangle - \langle (U - B)_{\text{gal}} \rangle$ is also reported.

where $dN_{\text{AGN}}(L_X|M_*, z)$ is the observed number of AGN in each bin of X-ray luminosity, stellar mass and redshift and we have defined:

$$d\bar{N}_{\text{gal}}(M_*, z) = \frac{1}{dN_{\text{AGN}}(L_X|M_*, z)} \sum_{i=1}^{dN_{\text{AGN}}} N_i(L_{X,i}|M_*, z). \quad (8)$$

$N_i(L_X|M_*, z)$ is the number of galaxies that could have been detected as X-ray sources at their position (given the known exposure map of the XMM-COSMOS survey) if they had the luminosity $L_{X,i}$ of the i th AGN in the given bin.

Figure 14 shows the probability of galaxies hosting AGN, p_{AGN} , for different stellar mass bins in three redshift intervals. For lower mass points, completeness has been treated conservatively, i.e. we have assumed that the parent galaxy sample is complete only

above the mass completeness limit for quiescent galaxies as function of redshift, as reported in Ilbert et al. (2010) (this translates into mass limits completeness of about $M_* = 10^{9.7}, 10^{10.1}, 10^{10.7}$ for the three redshift bins, respectively). In those cases, our AGN fractions are considered as upper limits.

The good statistics of our large, homogeneous and complete sample, allows for an accurate study of AGN incidence, which accounts for both redshift and intrinsic AGN luminosity dependence (see Aird et al. 2012). In each panel, AGN with different intrinsic X-ray luminosity are plotted with different colors. While the global trend with masses remains qualitatively the same in each luminosity bin, the normalization strongly decreases with luminosity, i.e. for a galaxy of a given mass the probability to host an AGN is

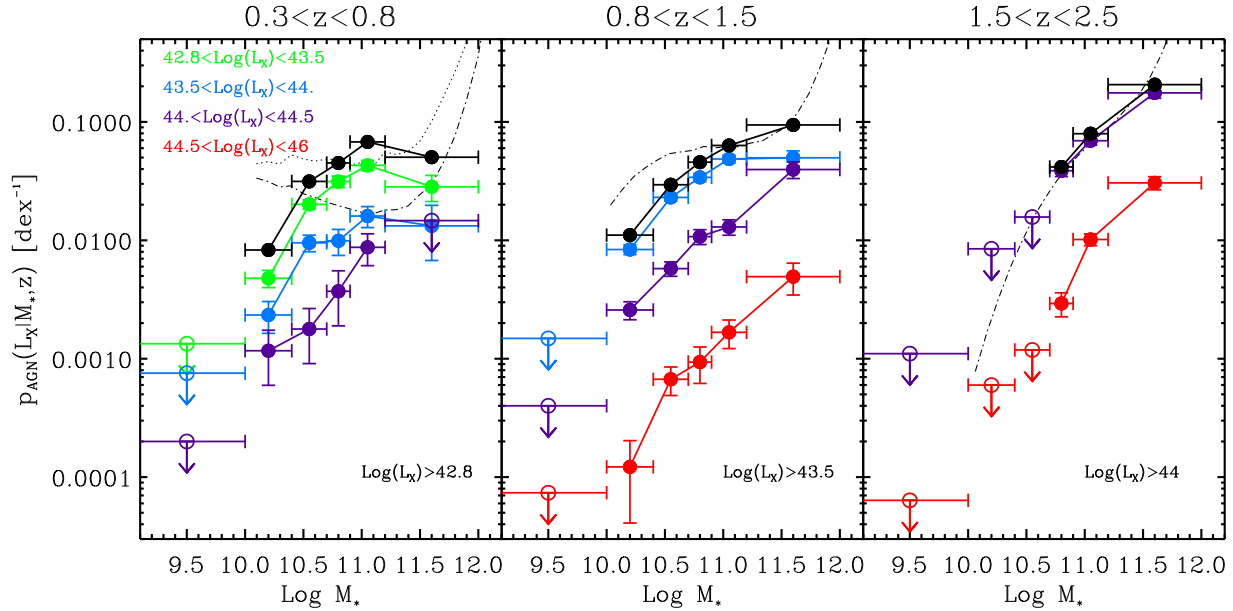


Figure 14. Probability of a galaxy to host an AGN of a given luminosity as a function of stellar mass in three redshift bins. Different colors show different X-ray luminosity bins: green for $\log(L_{[2-10\text{keV}]})=[42.8-43.5]$; blue for $\log(L_{[2-10\text{keV}]})=[43.5-44]$; purple for $\log(L_{[2-10\text{keV}]})=[44-44.5]$ and red for $\log(L_{[2-10\text{keV}]})=[44.5-46]$; the black points refer to the total fraction computed by summing all objects above the given luminosity thresholds. Upper limits correspond to the mass bins where the host galaxy parent sample is not complete, as determined by the completeness limits for quiescent galaxies in COSMOS reported in Ilbert et al. (2010). The thin dot-dashed line is the prediction for the total AGN fraction, computed in the same redshift bins, and above the same luminosity thresholds, from the “AGN occupation” model of Fiore et al. (2012) while the dotted line in the first redshift bin is a modified version of it (see text for more details).

higher as the AGN X-ray luminosity decreases and the same happens at any redshift. This is an obvious consequence of the shape of the AGN luminosity function: more luminous AGN are rare, while less luminous ones are much more common.

Very interestingly, as already shown by Aird et al. (2012), the $p_{\text{AGN}}(L_X|M_*,z)$ as a function of galaxy stellar mass do show very similar profiles at *all* sampled luminosities. AGN, of any intrinsic luminosity, are more common the more massive the host galaxy is. This is by no means a trivial fact: one could have easily expected that more luminous AGN were to be found in more massive galaxies and less luminous AGN in lower mass galaxies. This, in fact, is the prediction of any model in which black hole growth in AGN phases occurs over relatively narrow Eddington ratio ranges, and the very different picture we observe in Fig. 14 (as well as in Fig. 15, see below) is a strong indication that AGN of all masses should be characterized by a very broad distribution of Eddington ratios (see e.g. Merloni & Heinz 2008). We quantify this statement by studying the AGN fractions as a function of the specific accretion rate in section 4.3.2 below.

Figure 14 also shows (black points) the total AGN fraction above a given luminosity thresholds in each redshift interval (i.e. computed by summing up the $p_{\text{AGN}}(L_X|M_*,z)$ in different luminosity bins). As a comparison, the thin dot-dashed line is the prediction for the total AGN fraction, computed in the same redshift bins and above the same luminosity thresholds, from the “AGN occupation” model of Fiore et al. (2012). We refer the reader to that work for more details, but we note here that in Fiore et al. (2012) the AGN fraction is computed by deriving an active SMBH mass function from the observed AGN luminosity function, assuming a given shape for the Eddington ratio distribution, and then comparing it to the observed galaxy mass function. In the two highest redshift bins,

such a model reproduces our data remarkably well. However, severe discrepancies appear in our lowest redshift range. As we will show in the next section, it appears that the true Eddington ratio distribution of our AGN is better described by a simple power-law and the fact that the shape assumed in Fiore et al. (2012) is a log-normal can explain the discrepancy. In fact, while in the highest redshift bins, where our COSMOS AGN sample probes just a limited range of Eddington ratios, the observed distribution is hardly distinguishable from a log-normal distribution with appropriate parameters, in the lowest redshift range, the log-normal shape assumed by Fiore et al. (2012) under-predicts the number of low luminosity AGN hosted in massive galaxies ($10^{10.6} < M_* < 10^{11.6}$). Assuming a log-normal distribution with a peak at lower Eddington ratio would already improve the prediction in the first redshift bin as shown by the dotted line in Fig. 14 which corresponds to a distribution with $\lambda_{\text{peak}}=0.03$.

4.3.2 AGN fraction as a function of specific accretion rate

Indeed, by combining the available information (host galaxy stellar mass and AGN luminosity) we can study the probability of a galaxy to host an AGN as a function of mass in bins of “specific accretion rate”, i.e., the ratio L_X/M_* which gives an approximate estimate of the rate at which the SMBH grows. To the extent that a proportionality between the black hole mass and the (total) host galaxy stellar mass can be assumed (and this is far from being clear, see e.g. Merloni et al. 2010), this ratio could give a rough measure of the black hole Eddington ratio, defined as the ratio between the AGN X-ray luminosity and the Eddington luminosity. To be spe-

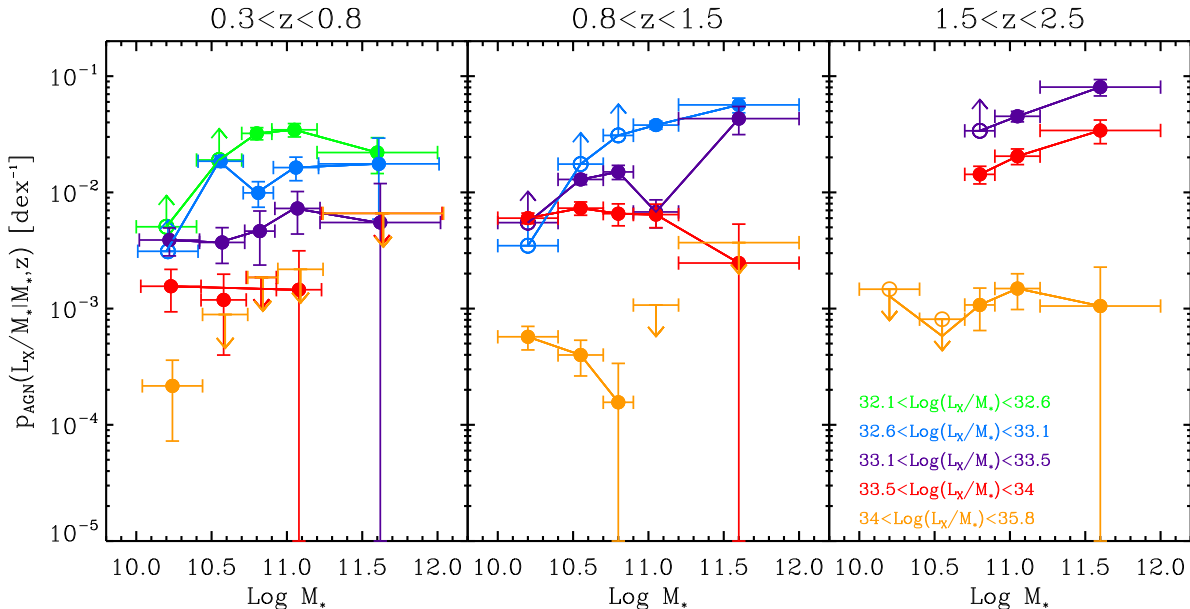


Figure 15. Probability of a galaxies to host an AGN per decade specific accretion rate (L_X/M_*) as a function of stellar mass in three redshift bins. Different colors show different L_X/M_* intervals, as explained in the third panel. Empty symbols with arrows show upper and lower limits due to the combined effect of completeness in both L_X and M_* . Upper limits without empty circles mark the bins where no AGN was found, and were placed using the Gehrels (1986) formulae for Poisson statistics.

sific, the Eddington ratio can be expressed as:

$$\lambda_{\text{Edd}} = \frac{\mathcal{A} \cdot k_{\text{bol}}}{1.3 \times 10^{38}} \times \frac{L_X}{M_*} \quad (9)$$

where k_{bol} is the 2-10 keV bolometric correction, and the factor \mathcal{A} is a constant if the SMBH mass can be related to the host galaxy mass through scaling relations (with $\mathcal{A} \approx 500\text{--}1000$; Häring & Rix 2004; Magorrian et al. 1998). Thus, for a mean bolometric correction⁹ of $k_{\text{bol}} = 25$ and a constant host stellar to black hole mass ratio of $\mathcal{A} = 500$, a ratio of $L_X/M_* = 10^{34}$ would approximately correspond to the Eddington limit.

Figure 15 shows how the probability $p_{\text{AGN}}(L_X/M_*|M_*, z)$ of a galaxy to host an AGN of a given specific accretion rate scales with the stellar mass of the host. Here, of course, the issue of completeness is far more complicated. Depending on the L_X/M_* ratio interval considered, both the flux limit of the X-ray survey and the stellar mass completeness limit of the parent galaxy sample should all be taken into account. Figure 15 shows that, at any given specific accretion rate (a proxy, with all the caveats discussed above, of the Eddington ratio), the trend with mass almost disappears: the probability for a galaxy to host an AGN of a given L_X/M_* is almost independent of its mass but scales only with the ratio itself.

In Figure 16, we then plot $p_{\text{AGN}}(L_X/M_*|M_*, z)$ as a function of the specific accretion rate itself. As mentioned above, there is little dispersion among the points corresponding to different mass bins for the same L_X/M_* interval. We can assume that the AGN fraction at any given value of the L_X/M_* ratio is independent of host galaxy mass, and measure such a constant “universal” mean probability for every specific accretion rate and redshift bin. The thick black triangles in Fig. 16 show the mean values of $p_{\text{AGN}}(L_X/M_*|M_*, z)$.

⁹ recent works (Lusso et al. 2010, 2011) have shown that the 2-10 keV bolometric correction is likely an increasing function of the Eddington ratio itself, a further complication that we here neglect.

Indeed, all the data seem consistent with the idea that, at every redshift, there is a *universal* distribution function that describes the probability of a galaxy of any mass (above our completeness limit of $\sim 10^{10} M_\odot$) to host an AGN of a given specific accretion rate L_X/M_* , independent of host stellar mass (Aird et al. 2012).

As we have anticipated, to the first order, the data are consistent with a power-law like distribution and a clear break at values of L_X/M_* consistent with the Eddington limit. In Table 2 we report the values of the best fit power-law distribution for each of the three redshift bins, in the form¹⁰:

$$p_{\text{AGN}}(L_X/M_*|M_*, z) = K \left(\frac{L_X}{M_*} \right)^{-\gamma} \quad (10)$$

As compared to the values found in Aird et al. (2012), we find a somewhat steeper slope for the power-law index (≈ 1 rather than ≈ 0.7). We speculate that this might have to do with the fact that, differently from Aird et al. (2012), we do not include AGN from the deepest *Chandra* fields, that probe the fainter, shallower end of the X-ray luminosity function. Hint of such a flattening can be seen in the decline of the p_{AGN} for the most massive galaxies at low X-ray luminosities in Fig 14. These are very low specific accretion rate objects for which we are not complete in the COSMOS sample (they are shown as lower limits in Figures 15 and 16) and therefore cannot properly assess the robustness of any change in slope at low

¹⁰ We note here that the fact that the *observed* distribution of specific accretion rates (or, for what matters, Eddington ratios) is typically found to be log-normal (see e.g. Kollmeier et al. 2006; Netzer 2009; Trakhtenbrot et al. 2011; Lusso et al. 2012), rather than a power-law, is due to the combined effects of a flux limited survey, that depletes the number of low specific accretion rates at progressively lower masses, and of the fact that very massive galaxies, where slowly accreting objects can be detected are exponentially rarer as the stellar mass increases. A thorough discussion of these selection effect on the determination of the accretion rate distribution function of AGN can be found in Schulze & Wisotzki (2010) and Aird et al. (2012).

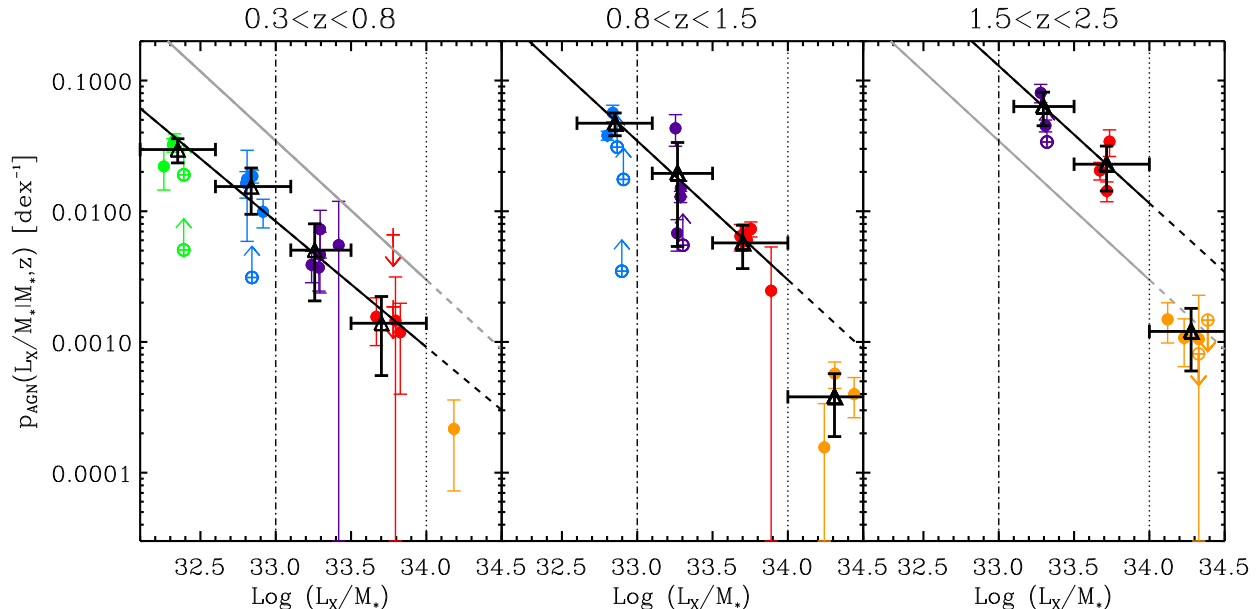


Figure 16. The probability of a galaxy to host an AGN of a given specific accretion rate (per decade L_X/M_* ratio) is plotted as a function of L_X/M_* for three redshift intervals. Colored points, have the same coding of Fig. 15 and plot the individual measurements, while black thick triangles are the mean values. The thick black line in each panel is a power-law fit to all the mean points obeying $\text{Log}(L_X/M_*) < 34$. For ease of comparison, in each panel we also show the best fit to the central redshift interval. The vertical dotted (dot-dashed) lines mark the approximate location of objects at the Eddington limit (or ten per cent of it) calculated assuming a constant bolometric correction $k_{\text{bol}} = 25$ and a constant host stellar to black hole mass ratio of $\mathcal{A} = 500$.

Table 2. The best fit slope and normalization for the universal probability distribution function $p_{\text{AGN}}(L_X/M_*, z)$ as a function of redshift for the entire X-ray selected sample, as shown in Fig. 16.

redshift range	all X-ray	
	Log K	γ
$0.3 < z < 0.8$	29.50	0.96
$0.8 < z < 1.5$	33.41	1.06
$1.5 < z < 2.5$	33.46	1.04

L_X/M_* . The possibility that the $p_{\text{AGN}}(L_X/M_*/M_*, z)$ might break to a shallower slope at low values of the specific accretion rate could be tested, indirectly, by comparing the observed X-ray luminosity function of the AGN with a convolution of the observed galaxy mass function and the probability distribution $p_{\text{AGN}}(L_X/M_*/M_*, z)$. We defer this investigation to a future work.

Nevertheless, we see very clearly in Fig. 16 that the $p_{\text{AGN}}(L_X/M_*/M_*, z)$ normalization increases with redshift over the entire redshift range probed by our data. If we compute the value of the $p_{\text{AGN}}(L_X/M_*/M_*, z)$ at $\text{Log}(L_X/M_*)=33.2$, i.e. at a specific accretion rate approximately corresponding to $\approx 10\%$ of the Eddington rate, and where our data best constrain the distribution at all redshifts, we find that it evolves with redshift as fast as the specific star formation rate of the overall population of galaxies (both star-forming and quiescent, see Karim et al. 2011) $\propto (1+z)^4$.

This very important fact, already pointed out, over a more limited redshift range, by Aird et al. (2012), implies that the rapidity with which a black hole grows is not influenced by the host galaxy mass, while, on the other hand, is a strongly evolving function of redshift, with a redshift dependence that follows the overall evolution of the specific star formation rate of the galaxy population. This also means that the trend with the hosts' mass visible in Fig. 14 and

widely confirmed by many authors before us, is a trend induced by the fact that in more massive galaxies we are able to detect AGN down to a lower intrinsic Eddington ratio, while in less massive galaxies only rapidly accreting black holes are bright enough to be observable, and their total number is therefore much smaller.

4.4 The incidence of AGN as a function of the star-forming properties of their hosts

Studies in the local Universe (Brinchmann et al. 2004; Salim et al. 2005) have pointed out the existence of two main galaxy populations: star-forming galaxies, which are currently forming stars at a rate that was found to be proportional to their mass, and quiescent galaxies, which are massive galaxies in which the star formation has been quenched¹¹. The specific star formation rate (sSFR) can be defined as the ratio, $\text{sSFR}=\text{SFR}/M_*$, of (total) star formation rate to stellar mass of a galaxy. The inverse of the sSFR defines a timescale for the formation of the stellar population of a galaxy, $t_{\text{SF}} = \text{sSFR}^{-1}$, which gives the time it would take a galaxy to double its stellar mass if forming stars at the observed rate.

In the sSFR vs mass plane, star-forming galaxies can be divided into a star-forming sequence (“main sequence” Noeske et al. 2007) characterized by an almost constant (or slightly decreasing) sSFR as a function of stellar mass, and a high mass region with progressively decreasing sSFR, the “dying sequence”, occupied by quiescent galaxies. In evolutionary terms, such a distribution is observed, almost unchanged, at any redshift, with the star-forming

¹¹ “Quenching”, regardless of its physical cause, is the process that cause the cessation of star formation in some star-forming galaxies, which leads to the emergence of the so-called red-sequence of passive galaxies (Strateva et al. 2001).

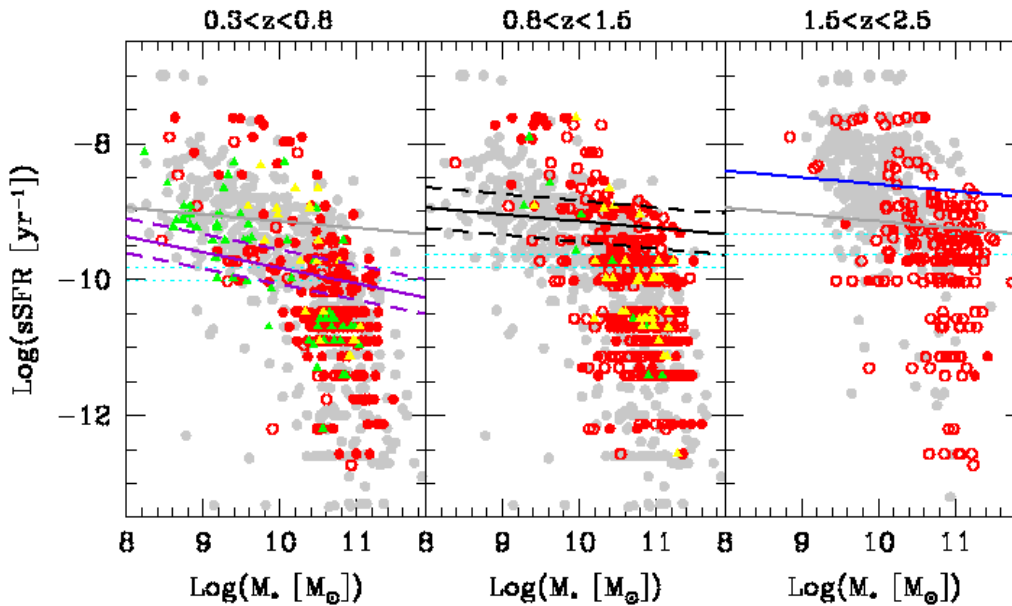


Figure 17. Specific star-formation rate versus stellar masses in three redshift bins for the host galaxies of type-2 AGN compared to normal galaxies from the i-band-apparent-magnitude-matched sample (gray points). The solid lines are the correlations found for blue star-forming galaxies: the purple one in the lowest redshift bin corresponds to $z \sim 0$ (Brinchmann et al. 2004), the black one in the intermediate redshift bin to $z \sim 1$ (Elbaz et al. 2007) and the blue one in the highest redshift bin to $z \sim 2$ (Daddi et al. 2007). In each panel the $z \sim 1$ curve is reported in grey for reference. The cyan dotted horizontal lines correspond to the age of the Universe $t_H(z)$ at the minimum and maximum redshift considered in each panel and indicate roughly the division between galaxies which are actively forming stars and quiescent.

galaxies sequence maintaining the same slope but increasing normalization as one moves towards higher redshift (Noeske et al. 2007; Elbaz et al. 2007; Daddi et al. 2007; Pannella et al. 2009). There are also more extreme objects, i.e. Starburst galaxies and Ultra Luminous Infrared Galaxies (ULIRGs), which exhibit highly elevated star formation rates (Sanders & Mirabel 1996) in galaxies within the same range of stellar mass of normal galaxies. Local ULIRGs are believed to be associated with rare major merger events (Sanders et al. 1988; Sanders & Mirabel 1996) and consequently distinct star formation processes, but recent studies with the *Herschel* telescope demonstrated that they represent a minor contribution to the total star formation rate density in the crucial redshift range $1.4 < z < 2.5$ (Rodighiero et al. 2011). Recent works (Wuyts et al. 2011) have shown that a detailed morphological analysis of galaxies as a function of their position in the sSFR-stellar mass plane can provide a unique insight on the physical processes that shape and grow galaxies, and how the various modes of star formation can be associated to them.

In light of the above results, it is obvious that a systematic study of the distribution of AGN host galaxies in the sSFR-stellar mass plane can reveal key pieces of evidence regarding the long sought-after association between SMBH growth and galaxy formation. Figure 17 shows the position of our obscured (type-2) COSMOS AGN host galaxies in the sSFR vs Mass plane compared to the overall non-AGN galaxy population (gray dots). We have purposely avoided to include type-1 objects in this diagram, as optical/UV-based SFR measures are too strongly affected by the unobscured accretion disc light in this class of AGN.

The purple, black and blue solid lines show the position of the main sequence at $z \sim 0$ (Brinchmann et al. 2004), $z \sim 1$ (Elbaz et al. 2007) and $z \sim 2$ (Daddi et al. 2007), while the cyan dotted lines correspond to the age of the Universe $t_H(z)$ at the min-

imum and maximum redshift considered in each panel. Galaxies of known redshift and sSFR can in fact be divided into “quiescent” and “star-forming” on the basis of their stellar mass doubling timescale, t_{SF} : if $t_{SF} < t_H(z)$, where $t_H(z)$ is the age of the Universe at the redshift of the source, the galaxy is defined as star-forming; if $t_{SF} > t_H(z)$ the galaxy is defined as quiescent. The i-band-apparent-magnitude matched parent galaxy population from the S-COSMOS survey (Ilbert et al. 2010) does indeed show a broad distinction between a star forming sequence and a dying sequence at the highest masses, which clearly evolves upwards (in sSFR) with increasing redshift.

Obscured AGN hosts, to a first order, appear to populate the high-mass end of the distribution quite uniformly. We estimate that the fraction of AGN hosted in starburst galaxies (defined as in Rodighiero et al. 2011 to be above 4 times the main sequence) is below 10% while the fraction of AGN hosted in main sequence galaxies range from 27% to 37% in the different redshift bins. The rest of the AGN (58%-66%) are found in quiescent galaxies. Considering only the most luminous sources as done by Mainieri et al. (2011), we found that at $z \sim 1$ about 62% of Type-2 QSOs were actively forming stars (i.e. hosted in starburst and main sequence galaxies). As comparison, Mullaney et al. (2012), using the FIR-*Herschel* data in the GOODS field and excluding the galaxies in which a strong contribution from the AGN to FIR wavelengths was evident, estimated for moderate luminous AGN the following percentages: <10% of AGN are hosted in strongly starbursting galaxies; 79% in main-sequence galaxies, and 15% in quiescent galaxies. The discrepancy between the two findings could be attributed to the differences (especially at low SFR) found between the SFR derived from SED fitting and the FIR ones as showed in Appendix B. To test this in detail, we fit below and above $20 M_{\odot}/\text{yr}^{-1}$ the SFR_{SED}-SFR_{IR} relation found (see left panel of Fig. B1) and we assign to

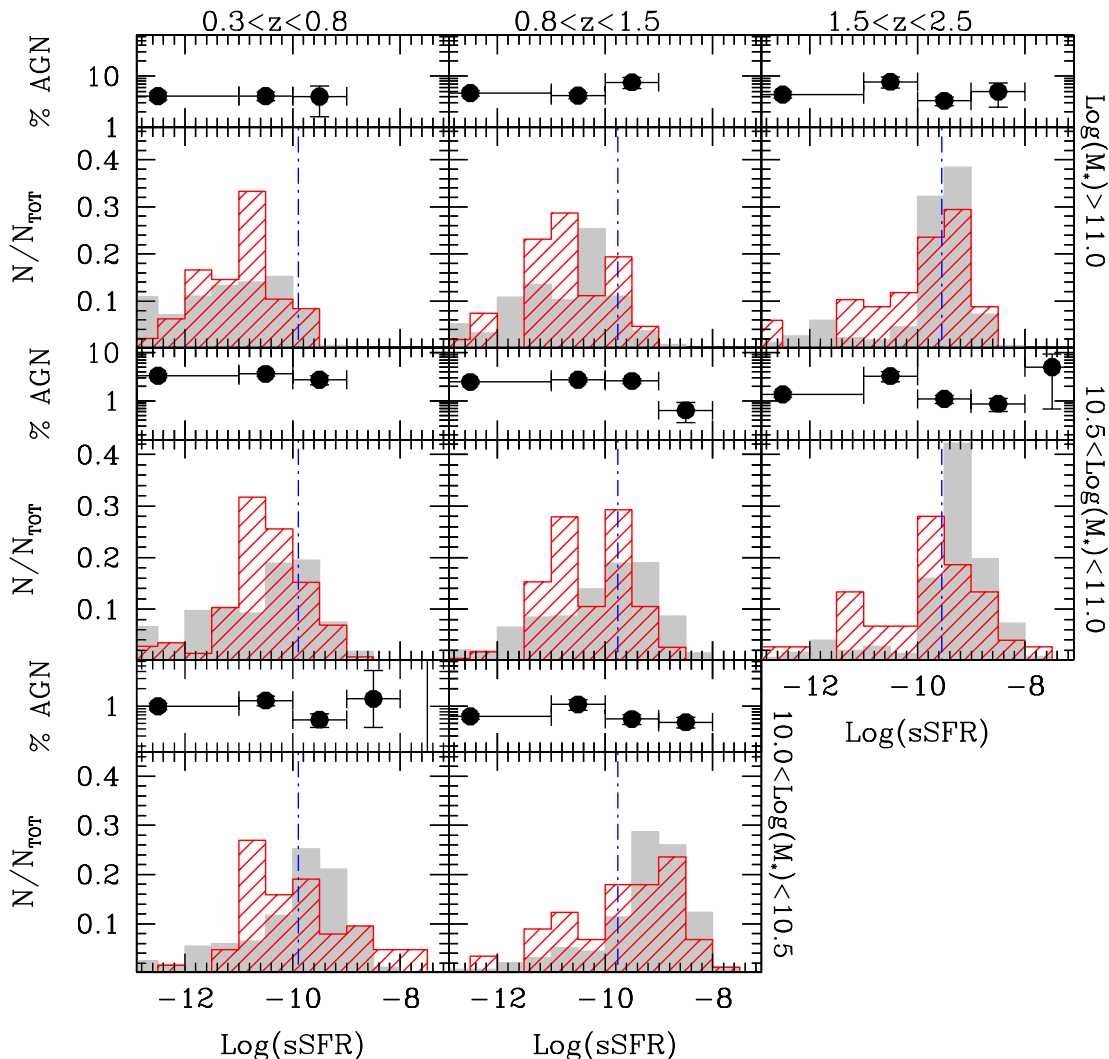


Figure 18. Specific star formation rate distributions divided in three redshift bins and three mass ranges for type-2 AGN host galaxies (red histogram) and normal galaxies (gray histogram). Dot-dashed vertical blue lines are used to distinguish quiescent from star-forming galaxies based on the ratio between the mass doubling time t_{SF} and the age of the Universe in any redshift bin. The upper panel of each histogram shows the observed AGN fractions.

each of our SFR values, the corresponding SFR_{IR} . We now find that the fraction of AGN hosted in strongly starbursting galaxies is 9%, while 67% are hosted in main-sequence galaxies, and 24% in quiescent galaxies, in much better agreement with the *Herschel*-based results.

Figure 18 shows, as histograms, the sSFR distributions of AGN hosts and normal galaxies in bins of stellar mass and redshift. Once again, the AGN do appear to follow the evolution of the specific star formation rate with stellar mass and redshift, with just a marginal increase in the AGN fraction towards lower values of sSFR in almost all bins, indicating a slightly higher incidence of (obscured) AGN in non-star-forming galaxies.

According to the models that assume that major mergers are the main AGN fueling mechanism (e.g. Hopkins et al. 2008), one could have expected an enhancement of the SFR activity in ob-

scured AGN, which is however not visible. From our analysis, there is no clear evidence that the COSMOS obscured AGN hosts are preferentially found among the extreme, most rapidly star-forming galaxies.

To analyze this in further detail we divide the host galaxies in two classes depending on the ratio between t_{SF} and t_{H} . According to this division of the total sample of obscured AGN discussed here, the fraction of quiescent hosts (always computed for stellar masses above the completeness limit of the COSMOS-IRAC survey, as discussed in Ilbert et al. 2010) are 75%, 65% and 61% in the redshift bins 0.3–0.8, 0.8–1.5 and 1.5–2.5, respectively. In total, about two thirds of the obscured AGN in COSMOS that we find in massive galaxies are hosted by objects with stellar mass doubling time longer than the age of the Universe. These fractions are higher than those of the galaxy sample, where the fraction of quiescent

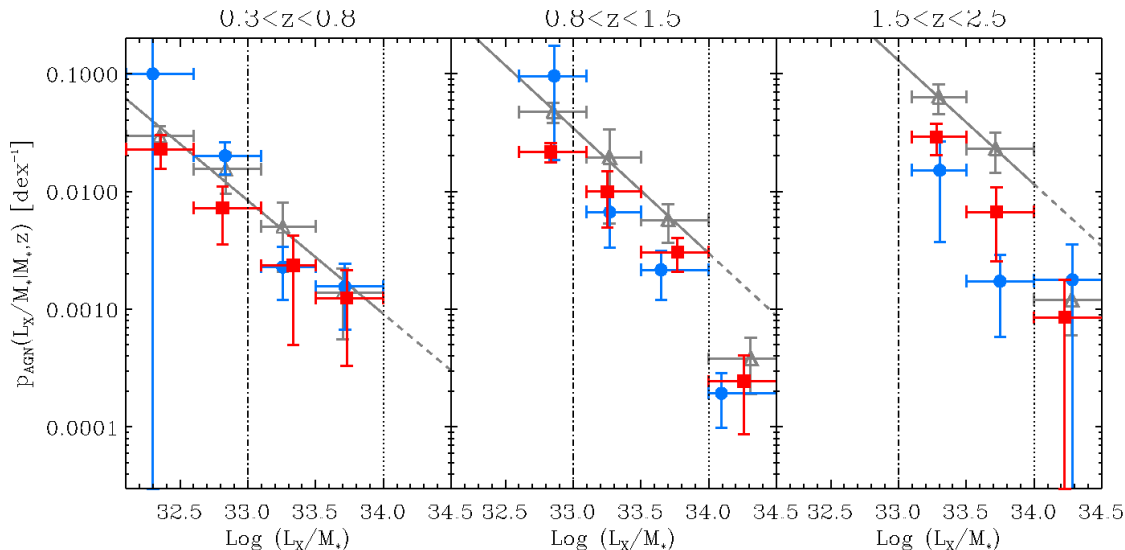


Figure 19. The average probability of a galaxy to host an AGN of a given specific accretion rate (per decade L_X/M_* ratio) is plotted as a function of L_X/M_* for three redshift intervals. In each panel blue filled circles are for star-forming galaxies (i.e. those with $t_{\text{SF}} < t_{\text{H}}$) and red squares are for quiescent ones (those with $t_{\text{SF}} > t_{\text{H}}$). Solid lines of corresponding colors show the power-law fit to all points obeying $\text{Log}(L_X/M_*) < 34$. The grey symbols and lines are the probability distribution functions for the overall galaxy population (for all AGN types), as from Fig. 16. The vertical dotted (dot-dashed) lines mark the approximate location of objects at the Eddington limit (or ten per cent of it) calculated assuming a constant bolometric correction $k_{\text{bol}} = 25$ and a constant host stellar to black hole mass ratio of $\mathcal{A} = 500$.

hosts are 51%, 41% and 32% in the redshift bins 0.3–0.8, 0.8–1.5 and 1.5–2.5, respectively. Such a predominance of quiescent (or, better, not strongly star forming hosts) is indeed consistent with the predominantly red colors exhibited by the AGN hosts that we discussed in section 4.1.

In section 4.3.2 we have computed the probability of a galaxy (above the stellar mass completeness threshold of the COSMOS-IRAC survey) to host an AGN of a given specific accretion rate, irrespective of the star-formation rate properties of the galaxies. For the sub-sample of AGN which are obscured, for which a reliable and robust determination of sSFR is possible, we have also computed separately the probability of star-forming and quiescent galaxies to host a (type-2) AGN as a function of specific accretion rate L_X/M_* . The results are shown in figure 19, where we also report, for the sake of comparison the overall p_{AGN} of Fig. 16. Taken at face value, the plot shows that there is little significant evidence for a difference in the probability of hosting a type-2 AGN in quiescent and star-forming galaxies, as the data points agree within the errors (that here are representative of the dispersion of $p_{\text{AGN}}(L_X/M_*|M_*, z)$ among the different stellar mass bins). The slight increase in the probability of hosting AGN in passive galaxies is hinted at in the highest redshift bin, while in the lowest one, star-forming galaxies appear to have a higher probability of hosting AGN with low specific accretion rate, but the number statistics is far too low to make any firmer statement. Even the size of our COSMOS sample is not large enough, once we subdivide the sources into spectral class, X-ray luminosity, stellar mass and star formation properties of the hosts.

5 DISCUSSION

Consistently with earlier studies, X-ray selected AGN are found to reside mainly in massive galaxies, while optically selected Seyfert-2 galaxies, which are also the low luminosity ones, seem to prefer

galaxies with smaller masses. The total stellar masses of the AGN host galaxies in our sample range from $10^{10}M_{\odot}$ to $10^{11.5}M_{\odot}$ with a peak at $10^{10.9}M_{\odot}$. No difference is found between X-ray obscured and unobscured AGN which on average show the same mass distribution.

In accordance with their high stellar masses, AGN hosts are more likely to be found in galaxies with red colors. Many authors have pointed out that the trend with color was just a mass driven effect and that removing the mass dependency would make it disappear (Silverman et al. 2009; Xue et al. 2010; Mainieri et al. 2011; Rosario et al. 2011). Indeed, several previous studies (e.g. Silverman et al. 2008) claimed that AGN were found mainly in a region of intermediate colors, the so called ‘green valley’. This was interpreted as evidence of a close association between the migration of galaxies from the ‘blue cloud’ to the ‘red sequence’ and the feedback from active nuclei. However, in most of these works, the AGN component was not subtracted in the computation of the host colors, and the dust extinction correction could not be properly assessed, leading to a possible blue contamination from the AGN and a higher incidence of AGN in the blue cloud and green valley. These two effects could explain our findings. In fact, in disagreement with the above studies, we find that compared to normal galaxies of the same mass, galaxies hosting an AGN are on average (slightly) redder and form stars less rapidly. It is only by properly taking into account both the dust extinction properties and the contamination from the nuclear light of the entire galaxy population that we can assess the true incidence of AGN as a function of star formation in their hosts. However, we cannot exclude that there is a difference in color between low luminosity AGN and intermediate-high luminosity ones and that this differences are, at least partially, responsible for the discrepancy between our result and previous studies based on deep fields (e.g. Silverman et al. 2008; Aird et al. 2012).

In agreement with the standard unified model (Antonucci 1993) and contrarily to what (maybe naively) expected from the

most popular models of AGN fueling and feedback (Hopkins et al. 2008), and with a number of caveats regarding the robustness of color determination in type-1 AGN, we do not find any significant difference between the host colors of obscured and unobscured AGN. We note here that recent works by Pierce et al. (2010) and Rosario et al. (2011) found possible evidence of a weak anti-correlation between the color of the AGN hosts and the hydrogen column density of X-ray obscuring gas N_{H} , in the sense that redder AGN seem to have on average higher values of N_{H} . As our classification into obscured and un-obscured AGN is a complex one, and mainly based on optical spectroscopy, it is not straightforward to compare our results with those of Pierce et al. (2010) and Rosario et al. (2011), but a common wisdom is emerging that (at least mildly) obscured AGN are not to be found among the most active star-forming galaxies.

When looking in detail at the relationships between AGN luminosity and host stellar masses, in agreement with Aird et al. (2012), we find that the probability to host an AGN of a given specific accretion rate L_{X}/M_* (a proxy for the SMBH Eddington ratio) is practically independent of the galaxy stellar mass, but depends strongly on redshift and on the specific accretion rate itself, i.e. there is a strongly decreasing probability to host an AGN with increasing L_{X}/M_* ratio.

This also means that the higher AGN fraction is observed in massive red galaxies simply because it is easier to detect the more prevalent, low Eddington ratio AGN in more massive galaxies, which are more likely to host the more massive SMBH.

The specific accretion rate distributions we can indirectly infer from the observed probability of a galaxy to host a AGN is better described by a power-law function, the slope and normalization of which appear to increase with redshift. We note here that Kauffmann & Heckman (2009), studying the present-day growth rates of black holes in SDSS galaxies using the [OIII] luminosity as a tracer of AGN accretion activity and stellar masses as tracer of the BH masses, pointed out the existence of two trends in the Eddington ratio distribution as a function of the stellar population (a ‘power-law’ and a ‘log normal’). These observed trends have been interpreted by them as the indication of two distinct accretion ‘modes’ for black holes: the log-normal distribution identifies a mode in which the supply of gas is ample (“feast”), while the power-law distribution corresponds to a mode where accretion is limited by the available supply of gas (“famine”). Another interpretation has been proposed by Hopkins et al. (2008), who identify the origin of the bi-modality in the evolution of triggering rates (mergers) in combination with a luminosity-dependent AGN lifetime. Our result shows that at higher redshift the picture might be different, as we do not find clear sign of a log-normal component in the specific accretion rate distribution, even when dividing the population of type-2 AGN hosts into actively star-forming and quiescent. This difference could be indicative of an interesting evolutionary effect to be further investigated, although we cannot exclude possible selection effect due to the fact that the work from Kauffmann & Heckman (2009) is based on a pure optically selected sample for which the AGN luminosity is computed based on the highly uncertain narrow line [OIII]-to-bolometric luminosity conversion. Nonetheless, the apparent universality of the observed probability distribution $p_{\text{AGN}}(L_{\text{X}}/M_*|z)$ suggests that, at least in the redshift range populated by our COSMOS sample, the same physical processes might be responsible for triggering and fueling AGN activity in galaxies of different masses.

We also find that the overall probability to host an AGN of any given L_{X}/M_* (as determined by the distribution normalization)

increases rapidly with redshift as $(1+z)^4$. Such an evolution can be due to either an increase in the number of sources accreting (vertical shift) or a shift of the characteristic Eddington ratio distribution towards higher values (horizontal shift). The second possibility would also explain the “AGN downsizing” (the comoving number density of high luminosity objects peaks at higher redshifts than low-luminosity AGN. La Franca et al. 2005; Hasinger et al. 2005; Bongiorno et al. 2007) as a consequence of the different Eddington ratio distribution at different redshift.

The fact that the probability of a galaxy to host an AGN of a given specific accretion rate evolves with redshift in the same way as the overall evolution of the specific star formation rate of the galaxy population (Karim et al. 2011) strongly suggests that AGN activity and star formation are globally correlated, at least in a statistical sense. From the physical point of view, the drop with time in the global star formation rate density reflects a drop in the availability of cold gas in galaxies to fuel star formation and potentially AGN. In that respect, AGN seem to follow the evolution of the galaxy population as a whole, a possibility reinforced by our detailed study of the position of AGN hosts in the sSFR-stellar mass diagram (section 4.4).

6 SUMMARY AND CONCLUSION

In this paper we studied a sample of ~ 1700 obscured and unobscured AGN, selected in the COSMOS field using X-ray and optical (spectroscopic) criteria. Of these, 602 are unobscured type-1 AGN (430 with spectra) and 1100 obscured type-2 AGN (549 with spectra) with L_{bol} ranging from 10^{43} to 10^{47} erg s^{-1} . Thanks to the wide COSMOS multi-wavelength coverage we were able to study in detail the source SEDs and to fit the observed fluxes with a two component model based on a combination of AGN and host-galaxy templates, accounting for dust extinction in both components independently. This method allowed us to decompose the entire spectral energy distribution into a nuclear AGN and a host galaxy component for almost all the sources and to derive robust measurements of both the AGN and the host galaxy properties (i.e. rest-frame colors, masses and SFRs). A test considering 1-component (galaxy) versus 2-components (galaxy+AGN) SED fitting technique, discussed in Appendix A, revealed that while considering only the galaxy component can be used to roughly estimate the blue colors of obscured AGN hosts, caution has to be used when deriving red magnitudes (e.g. M_K) and physical parameters, e.g. stellar mass and SFRs. On the contrary, for unobscured AGN hosts no study should be performed without properly taking into account the AGN component; even with this caution, we find that for unobscured AGN while total stellar masses of their host can be determined quite reliably, star-formation rate are too affected by nuclear light contamination to be deemed robust.

Our main findings can be summarized as follows:

- COSMOS AGN host galaxy masses range from $10^{10} M_{\odot}$ to $10^{11.5} M_{\odot}$ with a peak at $\approx 10^{10.9} M_{\odot}$. No significant difference is found in the stellar mass distributions of X-ray obscured and unobscured AGN hosts. Only optically selected Seyfert-2 galaxies without X-ray counterpart populate the tail in the distribution at lower masses down to $10^{8.5} M_{\odot}$.
- Host galaxies of obscured AGN span a very wide range of SFRs, with X-ray selected AGN populating the entire range, while optically selected Seyfert-2 galaxies being hosted mainly in galaxies with low SFRs (and very low masses). As extensively discussed in Appendix B, we find that above $\sim 20 M_{\odot} \text{yr}^{-1}$ the SFRs derived

from the SED and the one derived from the *Herschel* FIR observations are in good agreement. At low SFR ($< 20M_{\odot} \text{ yr}^{-1}$), however, the disagreement becomes evident, with our SED fitting method indicating substantially lower SFR than the FIR one.

We interpret this discrepancy as the possible combination of two effects: (i) contamination from star-formation-related emission in the NIR not properly taken into account in the SED fitting and (ii) AGN contamination in the FIR bands not taken into account in the FIR SFR estimates. We demonstrated that at least for the XMM-COSMOS sample, which is dominated by high luminosity AGN, the driven effect is the AGN contamination on the $60\mu\text{m}$ luminosities (see Appendix B for a detailed description), which, on the contrary, is low or even negligible for moderate and low luminosity AGN samples.

- In contrast to what was found by Cardamone et al. (2010), no clear bi-modality is seen in the color magnitude diagram of the COSMOS AGN hosts. At any redshift, the hosts of the AGN in our sample are mainly massive, redder galaxies. In many previous studies on AGN samples of much smaller size, AGN were found to have a higher incidence in star forming galaxies of blue colors (Silverman et al. 2009; Xue et al. 2010), once mass matched samples of active and non-active galaxies are considered. Even when accounting properly for the mass-color degeneracy, and when looking at mass-matched sample, we do not confirm these findings with our much improved statistics. Even at fixed stellar masses, well above the completeness limit of the COSMOS sample, we find a slight trend for AGN hosts to be redder (by ~ 0.1 – 0.2 magnitudes) than the non active galaxies. We argue that the main reason for such a discrepancy is the proper subtraction of the AGN light from our SED decomposition technique, complemented by a uniform and systematic treatment of dust extinction in both parent and AGN host galaxy sample. We caution, however, that degeneracies in color-magnitude diagrams may easily arise due to alternative choices of spectral templates and residual issues with the AGN-host decomposition technique.

- For a galaxy of any given mass above the stellar mass completeness limit of the COSMOS survey, the probability to host an AGN of a given X-ray luminosity increases with stellar mass, and this holds true for any value of the X-ray luminosity we are sensitive to. In fact, against the naive expectation that more luminous AGN should be found in more massive galaxies and less luminous ones in lower mass galaxies, we find that AGN of any intrinsic luminosity are more common the more massive the galaxy is.

- We have used the observable “specific accretion rate”, i.e. the ratio between X-ray luminosity and host galaxy stellar mass as a proxy for the Eddington ratio of the growing black hole. By doing so we find that the probability for a galaxy to host an AGN of any given Eddington ratio (or specific accretion rate) is roughly independent of the host galaxy stellar mass, but strongly decreases with increasing L_X/M_* , and we also found a clear evidence of a break in the specific accretion rate distribution at values consistent with the Eddington limit. These results imply that the higher incidence of AGN observed in massive galaxies by essentially all multi-wavelength surveys is just a consequence of the fact that low specific accretion rate objects are more common than high specific accretion rate ones, and, at the same time, low L_X/M_* objects in low mass galaxies drop out of flux-limited AGN samples. This effect, closely associated to the broad Eddington ratio distribution of AGN was anticipated in Merloni & Heinz (2008) and has been confirmed observationally by Aird et al. (2012).

- We found that the probability for a galaxy to host an AGN of any given specific accretion rate strongly increases with red-

shift, approximately as $(1+z)^4$ for SMBH accreting at about 10% of the Eddington limit, where most of the SMBH mass assembly is supposed to take place. Such a very strong evolutionary trend follows closely the overall evolution of the specific star formation rate of the galaxy population (Karim et al. 2011). This is yet another strong indication that AGN activity and star formation are globally correlated.

- To study in detail the star formation properties of the COSMOS AGN hosts, we have looked at the type-2 (obscured) AGN only, in order to avoid any bias/contamination from the inaccurate subtraction of the dominant blue nuclear light in type-1 objects. Type-2 AGN hosts have on average the same, or slightly lower SFRs than non active galaxies of the same mass and at the same redshift. We find that the fraction of AGN hosted in strongly starbursting galaxies is very low ($< 10\%$) while is higher for main sequence galaxies (27% to 37%) and quiescent ones (58%–66%). Compared to *Herschel*-based results (e.g. Mullaney et al. 2012), we find a much higher fraction of quiescent host. We tested that the discrepancy between the two results is explained by the differences in the SFR (especially below $20 M_{\odot} \text{ yr}^{-1}$) derived from SED fitting and FIR which have been attributed to the combination of the two opposite effects explained above.

The probabilities of star-forming or quiescent galaxies to host a type-2 AGN also decline as a power-law as a function of specific accretion rate and there are tantalizing hints of difference in the two populations and in their redshift dependence. However, more detailed investigations of the incidence of AGN in galaxies as a function of redshift, stellar mass, star-formation rate and nuclear luminosity are hampered by the limited statistics of the sample. Wide area surveys probing volumes at $z > 1$ comparable to that explored by SDSS in the local Universe will be needed to properly address the fundamental questions on the physical nature of the AGN-galaxy co-evolution.

The most striking piece of evidence that emerges from our study is the fact that AGN hosts do follow quite closely the overall evolution of the stellar build-up of the parent galaxy population and populate both star-forming and more passive galaxies almost equally.

We argue that, on the basis of the evidence presented in this work, it is hard to find strong indication that AGN play a direct role in shaping the global properties of their host galaxies, or their evolution. The same, probably stochastic, process of AGN activation and triggering seems to be in place in galaxies of all masses, with a slight predominance in red ones with specific star formation rates below the nominal threshold that distinguish actively star-forming from quiescent galaxies. Because of the robustness of this picture across the wide redshift range probed, we believe that whatever physical process is responsible for triggering and fueling AGN activity, it must be the same between $z \sim 2.5$ and $z \sim 0.3$, but must decrease in frequency or shift towards lower accretion rates. Although AGN activity and star formation appear to have a common triggering mechanism, we do not find strong evidence of any ‘smoking gun’ signaling powerful AGN influence on star forming galaxies SFR. The extent to which this lack of evidence can be meaningfully used to constrain and/or rule out theoretical models of AGN feedback, remains to be investigated.

ACKNOWLEDGMENTS

We thank the referee Dr. James Mullaney for the constructive comments which helped improving the manuscript and for the

interesting discussion. We also thank R. Hyckox and K. Schawinski for the useful discussions. AB work is supported by the INAF-Fellowship Program. The HST COSMOS Treasury program was supported through NASA grant HST-GO-09822. This work is mainly based on observations obtained with XMM-Newton, an ESA Science Mission with instruments and contributions directly funded by ESA Member States and the USA (NASA), and with the European Southern Observatory under Large Program 175.A-0839, Chile. In Germany, the XMM-Newton project is supported by the Bundesministerium für Wirtschaft und Technologie/Deutsches Zentrum für Luft und Raumfahrt (BMW/DLR, FKZ 50 OX 0001), the Max-Planck Society, and the Heidenhain-Stiftung. In Italy, the XMM-COSMOS project is supported by ASI-INAF grants I/009/10/0 and ASI/COFIS/WP3110,I/026/07/0. Part of this work was supported by INAF PRIN 2010 'From the dawn of galaxy formation to the peak of the mass assembly'. We gratefully acknowledge the contribution of the entire COSMOS collaboration; more information on the COSMOS survey is available at <http://www.astro.caltech.edu/cosmos>.

References

- Aird J. et al., 2012, *ApJ*, 746, 90
 Allevato V. et al., 2011, *ApJ*, 736, 99
 Antonucci R., 1993, *ARAA*, 31, 473
 Avni Y., 1976, *ApJ*, 210, 642
 Baldwin J. A., Phillips M. M., Terlevich R., 1981, *PASP*, 93, 5
 Barvainis R., 1987, *ApJ*, 320, 537
 Berta S. et al., 2011, *A&A*, 532, A49
 Best P. N., Kauffmann G., Heckman T. M., Brinchmann J., Charlot S., Ivezić Ž., White S. D. M., 2005, *MNRAS*, 362, 25
 Bongiorno A. et al., 2010, *A&A*, 510, A260000+
 Bongiorno A. et al., 2007, *A&A*, 472, 443
 Brandt W. N., Hasinger G., 2005, *ARAA*, 43, 827
 Brinchmann J., Charlot S., White S. D. M., Tremonti C., Kauffmann G., Heckman T., Brinkmann J., 2004, *MNRAS*, 351, 1151
 Brusa M. et al., 2010, *ApJ*, 716, 348
 Brusa M. et al., 2009a, *ApJ*, 693, 8
 Brusa M. et al., 2009b, *A&A*, 507, 1277
 Bruzual G., Charlot S., 2003, *MNRAS*, 344, 1000
 Calzetti D., Armus L., Bohlin R. C., Kinney A. L., Koornneef J., Storchi-Bergmann T., 2000, *ApJ*, 533, 682
 Capak P. et al., 2007, *ApJS*, 172, 99
 Cappelluti N. et al., 2009, *A&A*, 497, 635
 Cardamone C. N., Urry C. M., Schawinski K., Treister E., Brammer G., Gawiser E., 2010, *ApJL*, 721, L38
 Cen R., Chisari N. E., 2011, *ApJ*, 731, 11
 Chabrier G., 2003, *PASP*, 115, 763
 Chary R., Elbaz D., 2001, *ApJ*, 556, 562
 Cimatti A., Daddi E., Renzini A., 2006, *A&A*, 453, L29
 Ciotti L., Ostriker J. P., Proga D., 2010, *ApJ*, 717, 708
 Cirasuolo M., Magliocchetti M., Celotti A., 2005, *MNRAS*, 357, 1267
 Cisternas M. et al., 2011, *ApJL*, 741, L11
 Comastri A., Brusa M., 2008, *Astronomische Nachrichten*, 329, 122
 Cowie L. L., Songaila A., Hu E. M., Cohen J. G., 1996, *AJ*, 112, 839
 Croton D. J. et al., 2006, *MNRAS*, 365, 11
 Czerny B., Elvis M., 1987, *ApJ*, 321, 305
 Daddi E. et al., 2007, *ApJ*, 670, 156
 Dickinson M., Papovich C., Ferguson H. C., Budavári T., 2003, *ApJ*, 587, 25
 Donley J. L. et al., 2012, *ApJ*, 748, 142
 Elbaz D. et al., 2007, *A&A*, 468, 33
 Elbaz D. et al., 2011, *A&A*, 533, A119
 Elvis M. et al., 2009, *ApJS*, 184, 158
 Elvis M. et al., 1994, *ApJS*, 95, 1
 Elvis et al., 2012, *ApJ*, submitted
 Ferrarese L., Merritt D., 2000, *ApJL*, 539, L9
 Fiore F. et al., 2003, *A&A*, 409, 79
 Fiore F. et al., 2012, *A&A*, 537, A16
 Fontana A. et al., 2006, *A&A*, 459, 745
 Franceschini A., Hasinger G., Miyaji T., Malquori D., 1999, *MNRAS*, 310, L5
 Gandhi P., Horst H., Smette A., Hönig S., Comastri A., Gilli R., Vignali C., Duschl W., 2009, *A&A*, 502, 457
 Gebhardt K. et al., 2000, *ApJL*, 539, L13
 Gehrels N., 1986, *ApJ*, 303, 336
 Genzel R. et al., 2008, *ApJ*, 687, 59
 Gilli R., Vignali C., Mignoli M., Iwasawa K., Comastri A., Zamorani G., 2010, *A&A*, 519, A92
 Granato G. L., De Zotti G., Silva L., Bressan A., Danese L., 2004, *ApJ*, 600, 580
 Grazian A. et al., 2007, *A&A*, 465, 393
 Hao H. et al., 2010, *ApJL*, 724, L59
 Hao H. et al., 2009, in *Bulletin of the American Astronomical Society*, Vol. 41, American Astronomical Society Meeting Abstracts #213, p. 471.05
 Häring N., Rix H., 2004, *ApJL*, 604, L89
 Hasinger G., 2008, *A&A*, 490, 905
 Hasinger G. et al., 2007, *ApJS*, 172, 29
 Hasinger G., Miyaji T., Schmidt M., 2005, *A&A*, 441, 417
 Hickox R. C. et al., 2009, *ApJ*, 696, 891
 Hopkins P. F., Hernquist L., Cox T. J., Di Matteo T., Robertson B., Springel V., 2006, *ApJS*, 163, 1
 Hopkins P. F., Hernquist L., Cox T. J., Kereš D., 2008, *ApJS*, 175, 356
 Hopkins P. F., Richards G. T., Hernquist L., 2007, *ApJ*, 654, 731
 Ilbert O. et al., 2009, *ApJ*, 690, 1236
 Ilbert O. et al., 2010, *ApJ*, 709, 644
 Isobe T., Feigelson E. D., Akritas M. G., Babu G. J., 1990, *ApJ*, 364, 104
 Johansson P. H., Burkert A., Naab T., 2009, *ApJL*, 707, L184
 Karim A. et al., 2011, *ApJ*, 730, 61
 Kauffmann G., Heckman T. M., 2009, *MNRAS*, 397, 135
 Kennicutt, Jr. R. C., 1998, *ARAA*, 36, 189
 Kocevski D. D. et al., 2012, *ApJ*, 744, 148
 Kollmeier J. A. et al., 2006, *ApJ*, 648, 128
 Kormendy J., Bender R., 2011, *Nature*, 469, 377
 Kormendy J., Richstone D., 1995, *ARAA*, 33, 581
 La Franca F. et al., 2005, *ApJ*, 635, 864
 La Massa S. M., Heckman T. M., Ptak A., Hornschemeier A., Martins L., Sonnentrucker P., Tremonti C., 2009, *ApJ*, 705, 568
 Lamareille F., Mouhcine M., Contini T., Lewis I., Maddox S., 2004, *MNRAS*, 350, 396
 Le Floc'h E. et al., 2009, *ApJ*, 703, 222
 Lehmer B. D. et al., 2007, *ApJ*, 657, 681
 Lilly S. J. et al., 2007, *ApJS*, 172, 70
 Lilly S. J. et al., 2009, *ApJS*, 184, 218
 Lusso E. et al., 2010, *A&A*, 512, A34
 Lusso E. et al., 2011, *A&A*, 534, A110
 Lusso et al., 2012, *MNRAS*, submitted

Lutz D. et al., 2011, *A&A*, 532, A90
Magnelli B., Elbaz D., Chary R. R., Dickinson M., Le Borgne D., Frayer D. T., Willmer C. N. A., 2009, *A&A*, 496, 57
Magnelli B., Elbaz D., Chary R. R., Dickinson M., Le Borgne D., Frayer D. T., Willmer C. N. A., 2011, *A&A*, 528, A35
Magorrian J. et al., 1998, *AJ*, 115, 2285
Mainieri V. et al., 2011, *A&A*, 535, A80
Marconi A., Hunt L. K., 2003, *ApJL*, 589, L21
Marconi A., Risaliti G., Gilli R., Hunt L. K., Maiolino R., Salvati M., 2004, *MNRAS*, 351, 169
McCracken H. J. et al., 2010, *ApJ*, 708, 202
McLure R. J., Dunlop J. S., 2001, *MNRAS*, 327, 199
Menci N., Fiore F., Puccetti S., Cavaliere A., 2008, *ApJ*, 686, 219
Merloni A., 2004, *MNRAS*, 353, 1035
Merloni A. et al., 2010, *ApJ*, 708, 137
Merloni A., Heinz S., 2008, *MNRAS*, 388, 1011
Miyaji T., Hasinger G., Schmidt M., 2000, *A&A*, 353, 25
Monaco P., Fontanot F., 2005, *MNRAS*, 359, 283
Mullaney J. R., Alexander D. M., Goulding A. D., Hickox R. C., 2011, *MNRAS*, 414, 1082
Mullaney J. R. et al., 2012, *MNRAS*, 419, 95
Nandra K. et al., 2007, *ApJL*, 660, L11
Netzer H., 2009, *MNRAS*, 399, 1907
Noeske K. G. et al., 2007, *ApJL*, 660, L43
Pannella M. et al., 2009, *ApJL*, 698, L116
Pierce C. M. et al., 2010, *MNRAS*, 408, 139
Polletta M. et al., 2007, *ApJ*, 663, 81
Pozzetti L. et al., 2007, *A&A*, 474, 443
Pozzi F. et al., 2010, *A&A*, 517, A11
Prescott M. K. M., Impey C. D., Cool R. J., Scoville N. Z., 2006, *ApJ*, 644, 100
Prevot M. L., Lequeux J., Prevot L., Maurice E., Rocca-Volmerange B., 1984, *A&A*, 132, 389
Richards G. T. et al., 2006, *ApJS*, 166, 470
Rodighiero G. et al., 2010, *A&A*, 518, L25
Rodighiero G. et al., 2011, *ApJL*, 739, L40
Rola C. S., Terlevich E., Terlevich R. J., 1997, *MNRAS*, 289, 419
Rosario D. J. et al., 2011, *ArXiv e-prints*
Rosario D. J. et al., 2012, *ArXiv e-prints*
Salim S. et al., 2005, *ApJL*, 619, L39
Salvato M. et al., 2009, *ApJ*, 690, 1250
Salvato M. et al., 2011, *ApJ*, 742, 61
Sanders D. B., Mirabel I. F., 1996, *ARAA*, 34, 749
Sanders D. B., Phinney E. S., Neugebauer G., Soifer B. T., Matthews K., 1989, *ApJ*, 347, 29
Sanders D. B. et al., 2007, *ApJS*, 172, 86
Sanders D. B., Soifer B. T., Elias J. H., Neugebauer G., Matthews K., 1988, *ApJL*, 328, L35
Santini P. et al., 2009, *A&A*, 504, 751
Santini P. et al., 2012, *A&A*, 540, A109
Schawinski K. et al., 2006, *Nature*, 442, 888
Schawinski K., Treister E., Urry C. M., Cardamone C. N., Simons B., Yi S. K., 2011, *ApJL*, 727, L31
Schulze A., Wisotzki L., 2010, *A&A*, 516, A87
Scoville N. et al., 2007, *ApJS*, 172, 1
Shankar F., 2009, *NewAR*, 53, 57
Shankar F., Weinberg D. H., Miralda-Escudé J., 2009, *ApJ*, 690, 20
Shao L. et al., 2010, *A&A*, 518, L26
Silk J., Rees M. J., 1998, *A&A*, 331, L1
Silverman J. D. et al., 2009, *ApJ*, 696, 396
Silverman J. D. et al., 2008, *ApJ*, 675, 1025

Smolčić V., 2009, *ApJL*, 699, L43
Smolčić V. et al., 2008, *ApJS*, 177, 14
Soltan A., 1982, *MNRAS*, 200, 115
Somerville R. S., Primack J. R., Faber S. M., 2001, *MNRAS*, 320, 504
Springel V., Di Matteo T., Hernquist L., 2005, *ApJL*, 620, L79
Stern D. et al., 2005, *ApJ*, 631, 163
Stern J., Laor A., 2012, *ArXiv e-prints*
Strateva I. et al., 2001, *AJ*, 122, 1861
Taniguchi Y. et al., 2007, *ApJS*, 172, 9
Thomas D., Maraston C., Schawinski K., Sarzi M., Silk J., 2010, *MNRAS*, 404, 1775
Tommasin S. et al., 2012, *ArXiv e-prints*
Trakhtenbrot B., Netzer H., Lira P., Shemmer O., 2011, *ApJ*, 730, 7
Tremaine S. et al., 2002, *ApJ*, 574, 740
Trump J. R. et al., 2009, *ApJ*, 696, 1195
Trump J. R. et al., 2007, *ApJS*, 172, 383
Ueda Y., Akiyama M., Ohta K., Miyaji T., 2003, *ApJ*, 598, 886
Wilkins S. M., Trentham N., Hopkins A. M., 2008, *MNRAS*, 385, 687
Wuyts S. et al., 2011, *ArXiv e-prints*
Xue Y. Q. et al., 2010, *ApJ*, 720, 368

APPENDIX A: 2-COMPONENTS VERSUS 1-COMPONENT SED FITTING

In this section we will discuss the differences between the measured galaxy parameters that one obtains when using the SED fitting with two components (AGN and galaxy) compared to what would be obtained ignoring the AGN component, as in other studies (e.g. Silverman et al. 2009; Rosario et al. 2011). The color code for the symbols in the figures is the same as used throughout paper.

A1 Rest-frame magnitudes and galaxy colors:

Rest frame magnitudes in any given band are computed integrating the rest-frame galaxy template found as best fit solution in the corresponding filter. They are thus related to the “type” of galaxy chosen as best fit (which can introduce a difference up to 4 magnitudes) and, more important, to the normalization of the template, which is directly related to the total flux emitted by the source. In case of obscured AGN, the total emission in the U- and B-bands ($\lambda_{\text{eff}} \sim 3800\text{\AA} - 4500\text{\AA}$) is hardly influenced by the nuclear emission which is, at these wavelengths, partially or entirely absorbed (see lower panels Fig. 3). For this reason the shape of the chosen galaxy at these wavelengths and the normalization of the template should not strongly change when considering (or not) the AGN component. In order to test the effect of using one or two components fitting, we re-run our code using only galaxy templates. As shown in Fig. A1, the U and B rest frame host galaxy magnitudes of obscured AGN with (e.g. U[SED_{AGN+GAL}]) and without (e.g. U[SED_{GAL}]) the AGN component lie on the one-to-one relation with a roughly symmetric scatter of about 0.4 magnitudes (red, yellow and green symbols). On the contrary, the correlation is much worse for unobscured AGN (blue circles) whose U- and B-band rest frame magnitudes with and without AGN can be up to more than 2 magnitudes different. Moreover, the spread is not symmetric and not using the AGN component always leads to a much brighter galaxy. This is due to the fact that unobscured AGN

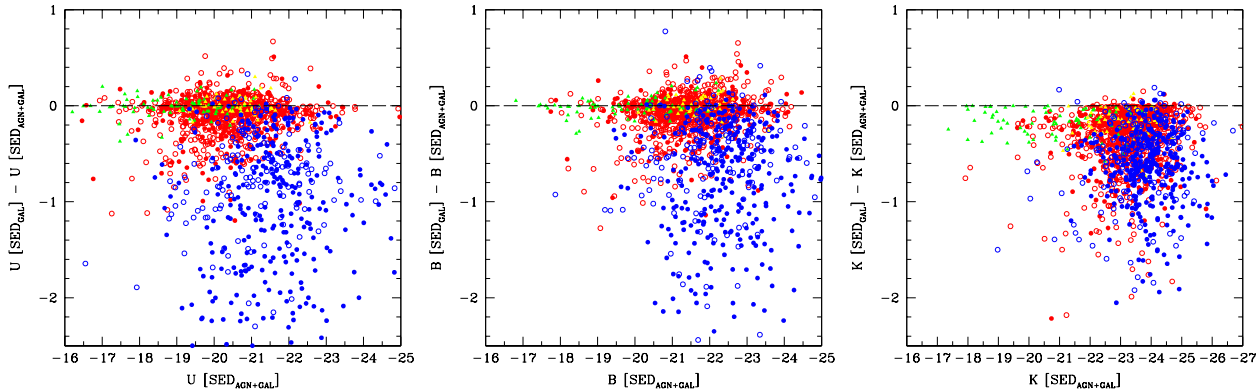


Figure A1. Comparison between the rest frame U-, B- and K-band magnitudes of our AGN host sample obtained using the 2-component SED fitting presented in this work versus the one obtained using a standard SED fitting considering only the galaxy component.

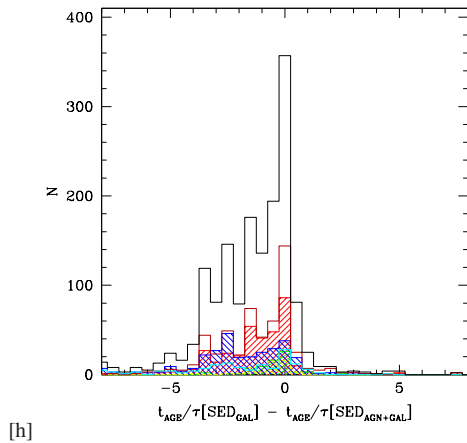


Figure A2. Comparison between the SED fitting parameters t_{age}/τ obtained using the 2-component SED fitting [GAL+AGN] presented in this work versus the one obtained using a standard SED fitting considering only the galaxy component.

emission is strong in the U and B bands (see upper panels of Fig. 3), i.e. not taking into account the AGN component corresponds to additional attributed flux to the galaxy hence resulting in an overestimation of the galaxy luminosity. The conclusion is different if we look at the comparison in the K-band ($\lambda_{eff} \sim 2.2 \times 10^4 \text{ \AA}$). Contrarily to the U- and B-band, at these wavelengths the contribution of AGN emission can be relevant even in the obscured sources (see e.g. the bottom right panel of Fig. 3). For this reason, the K-band magnitude of both obscured and unobscured AGN hosts will be overestimated (i.e. up to 2 magnitudes brighter) if we do not take into account the AGN component.

The objects whose host luminosities are less affected by the presence of an AGN component are the optically selected type-2 AGN without X-ray emission (triangles). For these objects the obscuration must be very high in order to suppress the AGN emission up to the K-band wavelengths. As suggested in Sec. 3.6, these sources are likely Compton-thick AGN and hence a high level of obscuration is expected.

A2 Host galaxy stellar mass and SFR

Apart from the rest-frame luminosity in various bands, the other two important parameters we derive from the SED fitting are the stellar masses and the star formation rates. Besides the dependence on the template normalization, these physical parameters are linked also to the principal parameters used in the SED fitting, i.e. the e-folding time (τ), the age since the beginning of star formation (t_{age}), and to some degree the extinction ($E(B-V)$). All SFHs considered in this work have an exponentially decreasing shape with $SFR \propto e^{-t_{age}/\tau}$ (but one, which is constant). For such an exponentially decreasing SFH, a large value of t_{age}/τ implies a quasi passive evolution with a negligible ongoing SF and that the majority of the stars in the galaxy are old (Grazian et al. 2007).

Fig. A2 shows the difference in the t_{age}/τ ratio when considering or not the AGN component in the SED fitting. In almost all cases, not considering the AGN component results in lower values of t_{age}/τ , which directly translates into galaxies with higher star formation rates, as visible in the right panel of figure A3. The right panel of this figure shows, for obscured type-2 AGN in the COSMOS sample, the ratio between the SFR obtained without the AGN component and once the AGN component is taken into account. For about 40% of the objects, the two values agree within a factor of 2, while for the rest of the objects the SFR estimated without AGN component is up to more than 20 times higher than the one obtained including the AGN.

Finally, the measured stellar masses show a non-negligible spread in both directions, for both obscured and unobscured AGN. As showed in the left panel of Fig. A3, the masses computed not including the AGN component range from 6 times higher (2 times if we consider only spectroscopic redshifts) to 10 times smaller (i.e. in unobscured AGN).

Summarizing, for obscured AGN a standard galaxy SED fitting technique that does not include a nuclear component results in small differences in rest frame U and B absolute magnitudes (~ 0.4 mag brighter) and larger ones for the K-band magnitudes (~ 0.8 mag brighter). The mass and SFR estimates are instead much more affected (up to a factor of 6 in mass, and SFR up to 20 times higher). This is not the case for optically selected type-2 AGN with no X-ray counterpart for which, due to the extremely high obscuration, the differences in magnitudes, mass and SFR are relatively small when considering (or not) the AGN component. For unobscured AGN on the contrary, all derived quantities (absolute magnitudes,

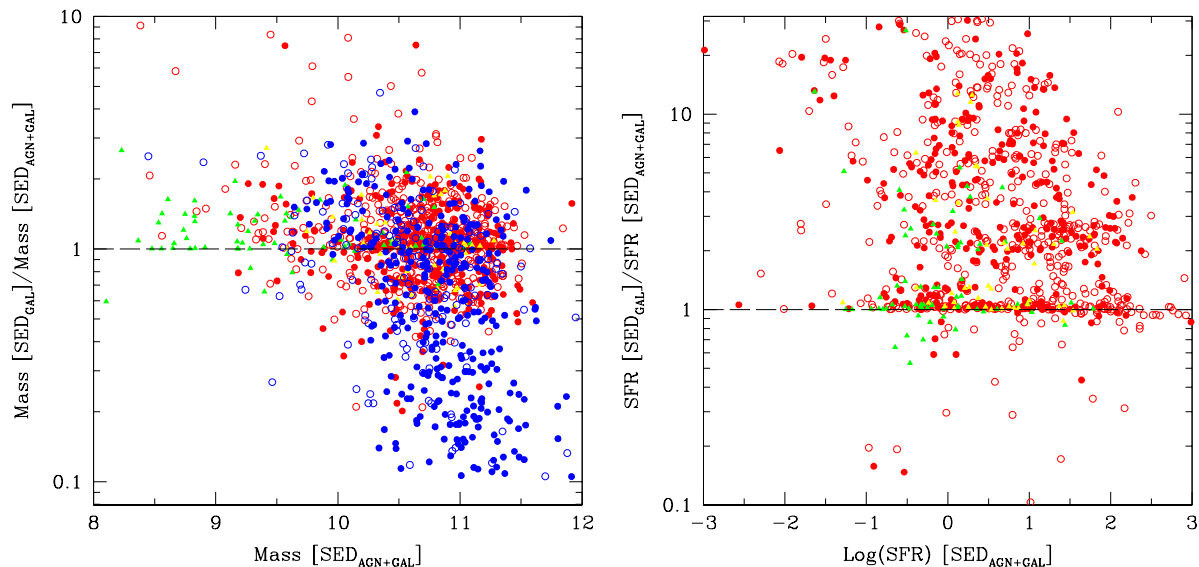


Figure A3. Comparison between the stellar masses and SFR of our AGN hosts obtained using the 2-component SED fitting presented in this work versus the one obtained using a standard SED fitting considering only the galaxy component.

stellar mass and SFR) are strongly offset from the values obtained when taking into account the AGN component.

In conclusion, while the SED fitting technique considering only the galaxy component can be used to roughly estimate the blue colors of obscured AGN hosts, caution has to be used when deriving red magnitudes (e.g. M_K) and physical parameters, e.g. stellar mass and SFRs. On the contrary, for unobscured AGN hosts no study can be performed without properly taking into account the AGN component.

APPENDIX B: COMPARISON BETWEEN DIFFERENT SFR INDICATORS

Evidences of star formation in galaxies can be seen in both the UV and IR bands. The UV emission is a direct measure of the starlight produced by a mixture of young (O, B and A type) stars. Using the UV emission to measure the SFR suffers from the limitation that part of the emitted radiation is absorbed, which is not taken into account. On the other hand, when using only the IR emission to constrain the SFR, the assumption is that a dominant fraction of the total bolometric stellar luminosity of the star-forming population is absorbed and re-radiated as thermal infrared dust emission. The most robust way to compute the SFR is thus the sum of both the unobscured UV star formation with the obscured one re-emitted in the IR by dust (SFR_{UV+IR}).

Thanks to the advent of the *Herschel* Space Observatory, deep far-infrared observations of the COSMOS field are now available. Here, we use the deep COSMOS PACS 100 and $160\mu\text{m}$ observations of the PACS Evolutionary Probe (PEP¹²; Lutz et al. 2011) guaranteed time key program, reaching a 3σ limit of ~ 4 mJy and ~ 10 mJy at 100 and $160\mu\text{m}$, respectively (see Berta et al. 2011). Using these observations we infer the obscured SFR of our host galaxies and test the accuracy of SFR derived from SED fitting.

Only a small fraction of our sources ($\sim 10\%$) are detected above the 3σ limits of the PEP catalogues. For these sources we computed the SFR using their infrared luminosities and assuming the L_{IR} to SFR conversion of Kennicutt (1998), i.e., $SFR = 10^{-10} L_{IR}$ for a Chabrier IMF. The IR luminosity L_{IR} is derived from the monochromatic luminosity at the longest PACS wavelength available converted using the infrared SED templates of Chary & Elbaz (2001) as it has been proven to provide reliable conversions over a broad range of redshift (Elbaz et al. 2011). In the left panel of Fig. B1 we show the comparison between the SFRs computed using the IR data and the one computed with the 2-components SED fitting. As visible, the majority of the sources lie above the 1 to 1 relation with the SFR computed from the SED being lower than the one derived from the IR. This is driven by a selection effect due to the fact that, given a broad distribution of SFR_{IR}/SFR_{SED} values, the Herschel detected sources will be the most powerful ones corresponding by definition to the upper envelope of the SFR_{IR}/SFR_{SED} distribution.

However, to test the accuracy of the SFR derived from SED fitting, we have to rely also on a statistical approach using a stacking analysis. Images of galaxies in a given redshift and SFR bin are stacked, allowing us to detect their typical far-infrared flux densities well below the detection limits of the current PACS observations (the noise of the stacked images scales roughly with the square root of the number of the stacked sources). We start by separate our galaxies into the usual three redshift bins (i.e., $0.3 < z < 0.8$, $0.8 < z < 1.5$ and $1.5 < z < 2.5$). Within each redshift bin, we then separate our galaxies per SFR bins. The size of the SFR bins are optimized in order to obtain the highest number of bins with clear PACS detections (i.e., $> 3\sigma$). The first SFR bin is initialized with a size of 0.1 dex and an upper range equal to the highest SFR observed in the redshift bin. Then, we progressively decrease the value of the lower range of the bin (using steps of 0.1 dex), until we obtain a 3σ detection in at least one PACS passband. The lower range of the bin is then taken as the upper range of the next SFR bin and the same procedure is repeated in order to find the size of the new bin. The process is stopped once the lower range of

¹² <http://www.mpe.mpg.de/ir/Research/PEP>

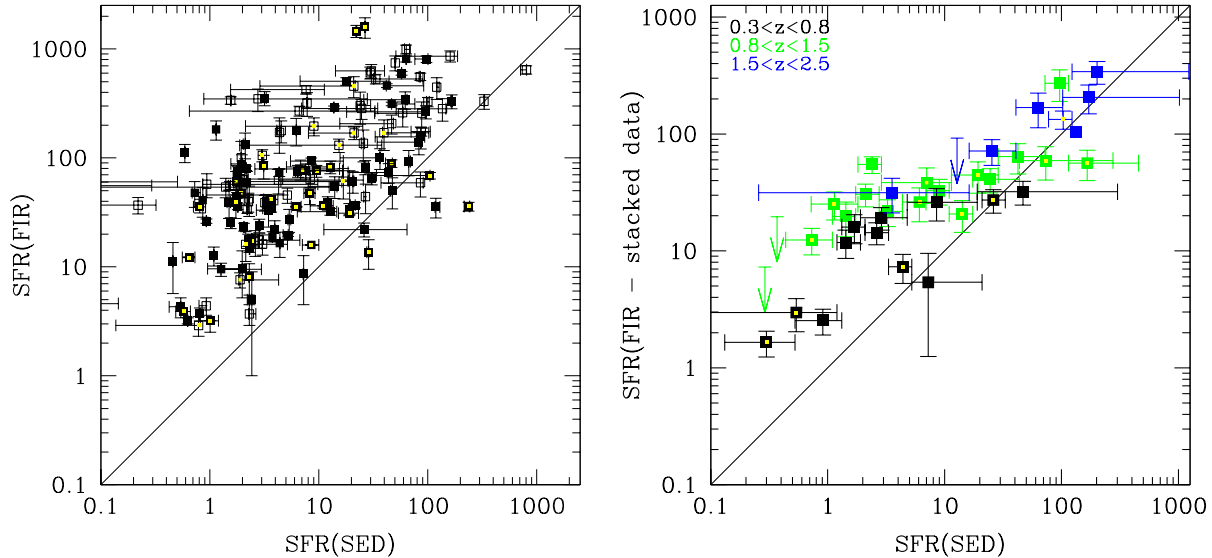


Figure B1. *Left:* Comparison between the SFR derived from the SED fitting and the one derived from the FIR band for the sources detected in at least one FIR band. Open and filled squares corresponds to objects with photometric and spectroscopic redshift respectively. *Right:* Comparison between the SFR derived from the SED fitting and the one derived from FIR using stacked data (binning in SFR_{sed} and redshift). Different colors correspond to different redshift ranges: $0.3 < z < 0.8$ black, $0.8 < z < 1.5$ green and $1.5 < z < 2.5$ blue.

the current bin reaches the lowest SFR observed in the redshift bin. Photometry of the stacked images are measured using the PSF fitting analysis presented in Magnelli et al. (2009, 2011) and using the relevant PSFs and aperture corrections of the COSMOS field (Berta et al. 2011). Errors are measured using a standard bootstrap analysis which takes into account both the photometric uncertainties of the stacked images and the intrinsic dispersion of the underlying galaxy population.

We derive the obscured SFR (i.e., SFR_{IR}) of each redshift and SFR bin using their stacked PACS flux densities and the Chary & Elbaz (2001) SED library. In the case where there is only one PACS detection (at $100 \mu\text{m}$ or $160 \mu\text{m}$), SFR_{IR} is obtained simply using the scaled Chary & Elbaz (2001) SED library. In the case where there are two PACS detections (at $100 \mu\text{m}$ and $160 \mu\text{m}$), we fit the PACS flux densities with the Chary & Elbaz (2001) SED library leaving the normalization of each template as a free parameter. In both cases, SFR_{IR} is given by integrating the best Chary & Elbaz (2001) SED template from 8-to- $1000 \mu\text{m}$ (L_{IR}) and using the standard SFR- L_{IR} relation of Kennicutt (1998) for a Chabrier (2003) IMF ($SFR [M_{\odot} \text{yr}^{-1}] = 1 \times 10^{-10} L_{\text{IR}} [L_{\odot}]$).

In the right panel of Fig. B1 we compare for type-2 AGN the SFRs computed using the stacked IR data and the one computed with the 2-components SED fitting. Above $\sim 20 M_{\odot} \text{yr}^{-1}$ the comparison is good with the SFR derived from the SED fitting being slightly underestimated, while at low SFR ($< 20 M_{\odot} \text{yr}^{-1}$) the disagreement becomes evident. This trend seems to be in contrast with previous studies which, however, were based on samples of normal galaxies. In fact, Santini et al. (2009) and Wuyts et al. (2011) studying a sample of galaxies at high redshift (up to $z \sim 3$) found an overall good correspondence between the $SFR_{\text{UV+IR}}$ and SFR_{SED} up to intermediate SFR, while at the largest SFR ($> 50 M_{\odot} \text{yr}^{-1}$) the discrepancy was significant and hence somewhat worrisome. However, Wuyts et al. (2011) showed that the deviation from a one-to-one relation between $SFR_{\text{UV+IR}}$ and SFR_{SED} is most severe for galaxies that have a large $SFR_{\text{IR}}/SFR_{\text{UV}}$ ratio which is not the

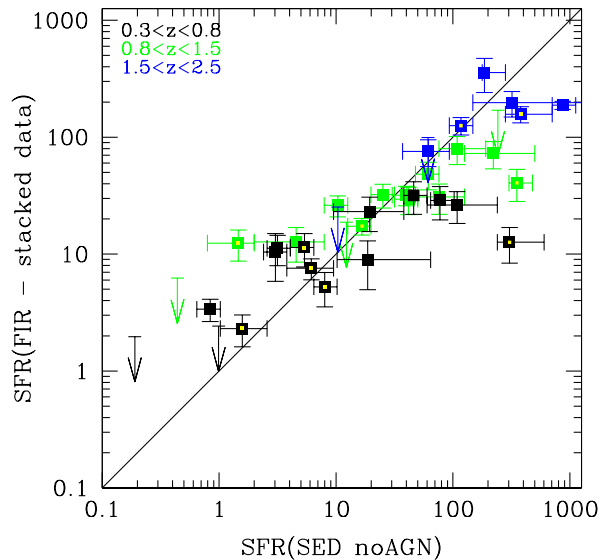


Figure B2. Comparison between the SFR derived from the SED fitting without AGN component and the one derived from FIR using stacked data (binning in SFR_{sed} and redshift). Different colors correspond to different redshift ranges: $0.3 < z < 0.8$ black, $0.8 < z < 1.5$ green and $1.5 < z < 2.5$ blue.

case for most of our sources (especially at high X-ray luminosities) for which the IR emission is dominated by the emission from hot dust heated by the AGN rather than young stars (see Sec. 3.6 and Fig. 8). However, for the sources for which this is not the case, we still assume that the IR band ($\sim 12 \mu\text{m}$ at $z \sim 1$) is dominated by the AGN emission and this assumption can lead to underestimate the SFR attributing the IR emission due to obscured young stars to the AGN component. On the other hand, the IR estimation of the SFR

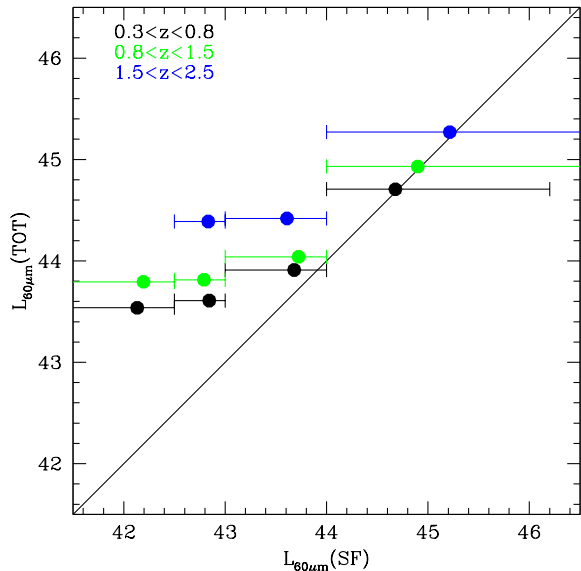


Figure B3. Mean total (AGN+SF) $L_{60\mu\text{m}}$ versus mean $L_{60\mu\text{m}}$ due only to the SF contribution obtained using a mock catalog of galaxies with different levels of SF and AGN contaminations (Rosario et al. 2012), statistically weighed using the observed L_{bol} distribution of our AGN sample in the usual three redshift bins. Error bars show the range in $L_{60\mu\text{m}}(\text{SF})$ used in the computation of the mean.

assume zero contamination from the AGN component in the IR and attribute the whole IR flux to the emission of the young stars. Again, this assumption, reasonable in most cases, can have the effect of overestimating the SFR, and the effect would be higher at low SFR where the contamination from the AGN is a significant fraction of the IR emission. As explained below, we performed two kinds of tests to explore the above hypotheses. First of all, we compared the SFR obtained from the SED fitting without including the AGN component with the IR SFR (see Fig. B2). We find that in this case there is a much better agreement between the two SFR indicators at low SFR. However, at high SFR we no longer have an agreement i.e. the SFR from the SED fitting is higher than the one derived from FIR band (Fig. B2). The result of this comparison indicates that the discrepancy seen in the right panel of Fig. B1 can be partly due to the fact that the SED fitting method tends to overestimate the AGN component thus under-predicting the SFR.

On the other hand, to test the AGN contamination to the FIR bands, we built a mock catalog of galaxies with different levels of SF and AGN contaminations¹³ From this catalog and using the computed weights, we calculated the average $L_{60\mu\text{m}}$ due to AGN+SF as a function of the $L_{60\mu\text{m}}$ due only to the SF. We find that, if we include the lowest luminosity tail of the AGN distribution i.e. AGN with L_{bol} down to 10^{41} erg s^{-1} , there is hardly any difference between the L_{SF} and L_{TOT} since the weighed mock is dominated

by low luminosity AGN. On the contrary, if we restrict the comparison to $L_{\text{bol}} > 10^{44}$ erg s^{-1} , we find that the $60\mu\text{m}$ luminosity is contaminated by the AGN contribution especially at low $L_{60\mu\text{m}}$. Since $L_{60\mu\text{m}}$ is commonly used as a proxy for L_{IR} and, therefore, SFR, this plot can be directly compared with Fig. B1 right panel. As clearly visible, the two plots show a very good agreement in the overall shape.

To perform a direct comparison with the observed trend in Fig. B1 right panel, we used the same mock catalog as before which this time is weighed using the observed L_{bol} distribution of our sample in the usual three redshift bins. The result is shown in Fig. B3 where the mean total (AGN+SF) $L_{60\mu\text{m}}$ versus the mean $L_{60\mu\text{m}}$ due only to the SF contribution are plotted. As clearly visible in the plot, the shape of the points in this figure and in our Fig. B1 right panel are in perfect agreement. This demonstrates that the trend observed when comparing SFR-IR and SFR-SED is mostly driven by the effect of AGN contamination on the $60\mu\text{m}$ luminosities. This effect is strong for the XMM-COSMOS sample, which is dominated by high luminosity AGN, but can be much smaller or even negligible when considering lower luminosity samples as demonstrated in the above test.

We conclude that the discrepancy seen in the right panel of Fig. B1 is due to the combination of two effects: (1) the SED fit tendency of overestimating the AGN component thus under-predicting the SFR and (2) the FIR-overestimation of the SFR especially at high AGN luminosities and low SFR, where the AGN contamination in the IR band is not negligible as demonstrated by the tests performed using the mock catalog.

APPENDIX C: AGN HOST GALAXY PARAMETERS DERIVED FROM THE 2-COMPONENT SED FITTING

Here we report as example the first 16 lines of the tables published online.

This paper has been typeset from a $\text{\TeX}/\text{\LaTeX}$ file prepared by the author.

¹³ intrinsic AGN luminosity at $60\mu\text{m}$ was estimated using the mean SED (normalized to the bolometric luminosity of the AGN) from Mullaney et al. (2011) and assuming a scatter around this value of 0.3 dex, which corresponds to the expected scatter in the SED shapes from Rosario et al. (2012). Since the simulation assumes that the AGN have a uniform distribution in AGN bolometric luminosity, we used the bolometric luminosity function of Hopkins et al. (2007) to derive statistical weights for the AGN sample depending on their L_{bol} and we applied them to get the real AGN distribution.

